Final Year Report for NASA Grant NAG-1-1472

Numerical Simulation of Shock/Turbulent Boundary Layer Interaction

Principal Investigator: Dr. Sedat Biringen
Phone : (303)492-2760
FAX : (303)492-7881

Research Associate: Dr. Ferhat F. Hatay
Phone : (303)492-3939
FAX : (303)492-7881

Department of Aerospace Engineering Sciences
University of Colorado
Boulder, Colorado 80309

NASA Technical Monitor: Dr. William E. Zorumski
Acoustics Division

ABSTRACT

Most flows of aerodynamic interest are compressible and turbulent. However, our present knowledge on the structures and mechanisms of turbulence is mostly based on incompressible flows. In the present work, compressibility effects in turbulent, high-speed, boundary layer flows are systematically investigated using the Direct Numerical Simulation (DNS) approach. Three-dimensional, time-dependent, fully nonlinear, compressible Navier-Stokes equations were numerically integrated by high-order finite-difference methods; no modeling for turbulence is used during the solution because the available resolution is sufficient to capture the relevant scales.

The boundary layer problem deals with fully-turbulent compressible flows over flat geometries. Apart from its practical relevance to technological flows, turbulent compressible boundary layer flow is the simplest experimentally realizable turbulent compressible flow. Still, measuring difficulties prohibit a detailed experimental description of the flow, especially in the near-wall region. DNS studies provide a viable means to probe the physics of compressible turbulence in this region.

The focus of this work is to explore the paths of energy transfer through which compressible turbulence is sustained. The structural similarities and differences between the incompressible and compressible turbulence are also investigated. The energy flow patterns or energy cascades are found to be directly related to the evolution of vortical structures which are generated in the near-wall region. Near-wall structures, and mechanisms which are not readily accessible through physical experiments are analyzed and their critical role on the evolution and the behavior of the flow is documented extensively.

1 INTRODUCTION

Apart from its practical relevance to technological flows, the turbulent compressible boundary layer flow is one of the simplest experimentally realizable turbulent compressible flows. Still, measuring difficulties prohibit a detailed description of compressible turbulence, especially in the near-wall region. Typically, the measurements are limited to the region above 0.1 boundary layer thickness, excluding the near-wall region (Kistler 1959, Spina, Donovan & Smits 1991). The lack of reliable data in the near-wall region where practically most of turbulence production and turbulence dissipation take place significantly retards the development of a theory of compressible turbulence. The focus of this paper is to provide a detailed description of compressible turbulence in supersonic boundary layers through direct numerical simulations as an adjunct to experimental observations.

Numerical simulations of compressible turbulence have been used to investigate simple flows in the recent years. Passot & Pouquet (1987) performed two-dimensional simulations of compressible, homogeneous turbulent flow for Reynolds numbers (based on a characteristic length of the medium and mean velocity) up to 500 and Mach numbers (based on fluctuating velocity field) of up to 2. Their computational results showed that for Mach numbers smaller than 0.3 the flow remains quasi-incompressible. Porter, Pouquet & Woodward (1992) performed a three-dimensional simulation of supersonic, homogeneous turbulence and studied the formation of shocklets and their contribution to the vorticity production in the initial (transient) stages. Erlebacher, Hussaini, Kreiss & Sarkar (1990) also captured the formation of weak shocklets in the transient regime in their three-dimensional simulations. They showed that the flow does not necessarily remain quasi-incompressible at later times when the initial perturbation velocity field is solenoidal. Sarkar, Erlebacher, Hussaini & Kreiss (1991b) evaluated the statistical moments using this data base obtaining correlations for compressible turbulence models. Feiereisen, Reynolds & Ferziger (1981) performed a three-dimensional, direct simulation of compressible, turbulent homogeneous shear flow and concluded that this anisotropic flow is not influenced by the compressibility to a large extent. In their homogeneous shear flow simulations implementing incompressible initial conditions on the velocities, Sarkar, Erlebacher & Hussaini (1991a) obtained subdued growth of turbulent kinetic energy with increasing fluctuation Mach number as well as increasing root-mean-square (r.m.s.)

density fluctuations.

Although these previous computational studies have contributed significantly to the understanding of fundamental mechanisms of compressible turbulence, it is generally accepted that while homogeneous turbulence is ever decreasing, the homogeneous shear turbulence is ever growing, if not monotonously in time certainly homogeneously in space. The dynamics and structure of turbulence in flows of aerodynamic interest can be learned through the investigation of more realistic flow fields which are both anisotropic and inhomogeneous, and contain both turbulence production and the means to balance it.

Morkovin (1962) compiled a hypothesis based on the limited body of data stating that the direct effects of density fluctuations on turbulence behavior are small if the r.m.s. density fluctuation is small compared with the absolute (mean) density. Originally the hypothesis was advanced to explain time-averaged behavior and was thought to apply to boundary layers with the free stream Mach number less than five. As acoustic fluctuations do not assume a dominant role within the limits of the Morkovin hypothesis, the only apparent compressibility effect is due to the mean density gradient. In this regard, the hypothesis is a generalization of the "Reynolds Analogy" which applies to the heated, incompressible boundary layers. Bradshaw (1977) reviewed Morkovin's conclusions and extracted the safe limits for the applicability of the hypothesis which coincided with the usual definition of hypersonic limits. At the height of the conclusions from Morkovin and Bradshaw, several semi-empirical relationships can be built parallel to the incompressible formulations (Coles 1964) with the proper treatment of the density variation across the boundary layer. However, recent experiments (Smits, Spina, Alving, Smith, Fernando & Donovan 1989, Spina & Smits 1987) indicate interesting structural differences between the supersonic and subsonic boundary layers in the outer layers. Moreover, these experiments indicate that the Mach number gradient becomes very high near the wall (Smits et al. 1989). Consequently, it is possible that the fluctuating Mach number, which is a measure of density fluctuations, increases beyond unity in the near-wall region where turbulent production and dissipation peaks. The turbulence structure and the role of organized motions which are well-documented in incompressible flows can potentially be even more significant in the compressible supersonic boundary layers. The coupling and interaction of near-wall structures with the outer layer structures can be different in the supersonic flows than the

subsonic flows. An assessment and investigation of these issues comprise the focus of the present work.

2 GOVERNING EQUATIONS

We consider viscous compressible flows governed by the Navier-Stokes equations and the thermodynamic equation of state. The fluid medium is assumed to be a heat-conducting perfect gas and a Cartesian frame of reference is considered (Figure 1). In what follows, free-stream values are denoted by subscript $()_\infty$ and superscript $()^*$ is used for dimensional quantities. The velocity vector is $\mathbf{u} = (u, v, w)$ and scalar flow variables are density ρ, temperature T, and pressure p. Displacement thickness,

$$\delta_1 = \int_0^\infty \left(1 - \frac{\rho^* u^*}{\rho_\infty^* u_\infty^*}\right) dy, \tag{1}$$

is used as the length scale in the nondimensionalization because, apart from its physical relevance, it is easier to control this quantity during the numerical simulations. Time, velocity, density, pressure and temperature are scaled with δ_1/U_∞^*, U_∞^*, ρ_∞^*, $\rho_\infty^* {U_\infty^*}^2$, and T_∞^* respectively. Thermophysical properties, viscosity and heat conductivity (μ^* and k^*), are also scaled with their respective values in the free-stream. The governing equations can be expressed in vector form using dimensionless variables as:

$$\frac{\partial \rho}{\partial t} + \nabla \bullet (\rho \mathbf{u}) = 0, \tag{2}$$

$$\frac{\partial \rho \mathbf{u}}{\partial t} + \nabla \bullet (\rho \mathbf{u} \circ \mathbf{u}) = -\nabla p + \nabla \bullet \boldsymbol{\tau}, \tag{3}$$

$$\frac{\partial E_T}{\partial t} + \nabla \bullet [(E_T + p)\mathbf{u}] + \nabla \bullet \mathbf{q}^* = \nabla \bullet (\boldsymbol{\tau}\mathbf{u}), \tag{4}$$

$$p = \rho \mathcal{R} T, \tag{5}$$

where $\bullet$ represents the vector/tensor inner product while $\circ$ is the outer product operation. Total energy per unit mass, E_T, and viscous stress tensor, $\boldsymbol{\tau}$, are defined as:

$$E_T = \rho \left(\frac{1}{\gamma(\gamma-1)M^2} T + \frac{u^2 + v^2 + w^2}{2}\right) \tag{6}$$

$$\boldsymbol{\tau} = \frac{\mu}{Re}[\nabla \mathbf{u} + (\nabla \mathbf{u})^T] + \frac{\lambda}{Re}(\nabla \bullet \mathbf{u})\mathbf{I}. \tag{7}$$

In the equations above $()^T$ is the transpose operator, and $\mathbf{I}$ is the identity matrix. Also, λ is the second coefficient of viscosity and is assumed to obey Stokes hypothesis, i.e.

$$\mu + 3/2\lambda = 0. \tag{8}$$

Heat-flux rate is denoted by $\mathbf{q} = (q_x, q_y, q_z)$ and is assumed to obey the Fourier law of heat conduction:

$$\mathbf{q} = -\frac{k}{RePrM^2(\gamma - 1)}\nabla T \tag{9}$$

Reynolds number, Mach number and Prandtl number are defined as:

$$Re = \frac{U^*_\infty \delta_1}{\mu^*_\infty / \rho^*_\infty} \quad M = \frac{U^*_\infty}{\sqrt{\gamma \mathcal{R} T^*_\infty}}, \quad Pr = \frac{\mu^*_\infty C^*_p}{k^*_\infty}. \tag{10}$$

Furthermore, $\mathcal{R} = C^*_p - C^*_v$ is the gas constant and the variation of the Prandtl number Pr, and specific heats C^*_p, C^*_v with temperature is neglected. In the present study, Pr and specific heat ratio $\gamma = C^*_p / C^*_v$ are taken to be 0.7 and 1.4 respectively. The dimensionless form of Sutherland's law for viscosity is expressed as:

$$\mu = k = T^{\frac{3}{2}} \frac{1 + S}{T + S}, \tag{11}$$

where $S = 110.4K/T^*_1$ and $T^*_1 = 288.15K$.

The present model neglects the streamwise growth of the boundary layer by assuming periodicity in this direction. The most important advantage of this assumption is the avoidance of artificial inflow/outflow conditions. Another benefit is the improvement of the statistical quantities of turbulence by allowing averaging along the streamwise direction. And still another significant gain is that one can use all the available computer resources to resolve one wavelength (or correlation length) thus improving the statistical accuracy. On the other hand, boundary-layer type solutions no longer satisfy the full Navier-Stokes equations under the streamwise-periodicity assumption. In order to obtain a shear profile as realistically close to the turbulent compressible boundary layer flow as possible, forcing functions are introduced into the x-momentum and energy equations as source terms on the right hand sides:

x-momentum:

$$f_x = \frac{\partial}{\partial y}\left(\frac{\mu_b}{Re}\frac{\partial u_b}{\partial y}\right), \tag{12}$$

Energy equation:

$$f_e = \frac{1}{PrM^2(\gamma-1)}\frac{\partial}{\partial y}\left(\frac{\mu_b}{Re}\frac{\partial T_b}{\partial y}\right) + \frac{\partial}{\partial y}\left(\frac{\mu_b}{Re}u_b\frac{\partial u_b}{\partial y}\right), \tag{13}$$

where the base profile is denoted by subscript $()_b$ and is obtained as the solution of turbulent compressible mean flow equations. Consistent with the parallel base flow assumptions, the only non-zero component of the base velocity is the streamwise component; the pressure is kept constant across the boundary layer. The same form of the forcing functions was also used by Erlebacher & Hussaini (1989) in their simulations of supersonic boundary-layer stability. It should be noted that this approach allows for the nonlinear distortion of the global mean motion when disturbances are introduced and imposes no restrictions on the evolution of the mean flow or of the fluctuations.

Periodicity is also imposed in the spanwise, z, direction. Along the y direction, no-slip and adiabatic conditions are imposed at the wall:

$$u = v = w = 0, \tag{14}$$

$$\frac{\partial T}{\partial y} = \frac{\partial p}{\partial y} = 0. \tag{15}$$

Along the top surface, zero-gradient (shear-free) condition is imposed on all variables:

$$\frac{\partial u}{\partial y} = \frac{\partial v}{\partial y} = \frac{\partial w}{\partial y} = 0, \tag{16}$$

$$\frac{\partial T}{\partial y} = \frac{\partial p}{\partial y} = 0. \tag{17}$$

3 COMPUTATIONAL APPROACH

The solution procedure used in the present work is the Two-Four method proposed by Gottlieb & Turkel (1976), as a fourth-order variant of the fully-explicit MacCormack method yielding fourth-order accuracy in space and second-order accuracy in time. The Two-Four scheme is highly phase-accurate and is very suitable for wave propagation and wave interaction problems (Biringen & Saati 1990). The allowable time step, Δt, for the current fully explicit method depends on the Courant Number (CFL) which is defined as:

$$CFL = \Delta t \underset{grid}{\text{maximum}} \left[\frac{|u|}{\Delta x} + \frac{|v|}{\Delta y} + \frac{|w|}{\Delta z} + a\sqrt{\frac{1}{\Delta x^2} + \frac{1}{\Delta y^2} + \frac{1}{\Delta z^2}} + 2\frac{vis}{Re}\left(\frac{1}{\Delta x^2} + \frac{1}{\Delta y^2} + \frac{1}{\Delta z^2}\right)\right], \tag{18}$$

where the term vis is given as,

$$vis = \frac{\max\left(\mu, \lambda + 2\mu, \frac{\gamma\mu}{Pr}\right)}{\rho}, \tag{19}$$

and a is the local speed of sound,

$$a = \sqrt{\frac{\gamma p}{\rho}}. \tag{20}$$

The stability of the numerical scheme is ensured for $CFL \leq 1$ and the scheme is optimized for $CFL \approx 2/3$.

Resolution Requirements

One reason for undertaking the DNS approach is that it is free from any assumptions of a turbulence model. For the very same reason, the resolution and the computational box size are crucial parameters to be determined in the direct simulations. Ideally, all relevant scales of the turbulent flow must be captured in all parts of the flow field. The resolution should be fine enough to resolve the finest scales of the turbulent motion while the domain should allow for the development of the largest turbulent structures.

Physical experiments on compressible boundary layers have revealed that large scale turbulent structures are of the same order of size (within a factor of 2) as the incompressible ones (Smits et al. 1989). Therefore in the present work, in choosing the dimensions of the computational box and grid resolution, the limits set by the previous incompressible DNS studies on turbulent wall-shear layers (Spalart 1988) was adopted; the final optimization was achieved through successive steps in an iterative procedure. Initial calculations were performed on a coarse grid with $(N_x \times N_y \times N_z) = (66 \times 64 \times 66)$ number of grid points in the x, y, and z directions, respectively. A high value for the Reynolds number was used (Re_{δ_1}=10,000) to excite the initial random disturbances of low amplitude (1%). The Mach number was initially set to 0.5 to prevent the formation of strong shock-waves during the first transients. The Mach number was then incrementally increased to 1.5 and then to 2.5, the supersonic values of eventual interest. After the initial transients were settled, Re_{δ_1} was reduced to 1000 and the resolution was incrementally increased to $258 \times 128 \times 130$ and subsequently to the final value of $386 \times 128 \times 258$. The flow field was interpolated from low-resolution grid to high resolution as needed. In the wall-normal direction, the final domain extends to $75\delta_1$ and there are approximately 11 points within 10 wall units which is more conservative than the previous transition and turbulence simulations of incompressible wall-shear layers.

Two simulations will be presented: the first one will be referred as **Case-Q1** and was performed at $M = 2.5$ and $Re_{\delta_1} = 1000$ at a resolution of $258 \times 128 \times 130$. The second simulation will be referred as **Case-Q2** and is a continuation of **Case-Q1** at a resolution of $386 \times 128 \times 258$. After the turbulence level was sustained in the simulations, the statistics were collected for a total time of $T = 187.2$ in **Case-Q1** over 31 and $T = 55.5$ in **Case-Q2** over 48 instantaneous data sets.

The temporal and spatial resolution level and the domain size used by Spalart (1988) and in the present work are given in Table 1 indicating that the present resolutions are comparable to previous incompressible DNS studies. Also included in Table 1 are the parameters used by Rai & Moin (1993) in the spatial simulation of low-Mach number transition to turbulence simulations, corresponding to the part of their domain where high resolution was employed to resolve the turbulence and sustain it. Different time-steps used in different studies are due to the different solution procedures and time-stepping algorithms employed.

Table 1: The computational domain size and the resolution used by Spalart (1988), Rai & Moin (1993), and by the present work. Γ corresponds to the total time used in the collection of statistics.

Study	M	Re_{δ_1}	$N_x \times N_y \times N_z$	L_x	L_y	L_z	Δx^+	Δz^+	Δt	Γ
Spalart-I	0	500	$128 \times 50 \times 96$	100	~ 130	25	20	6.7	0.3	200
Spalart-II	0	1000	$256 \times 64 \times 192$	100	~ 130	25	20	6.7	0.14	200
Spalart-III	0	2000	$432 \times 80 \times 320$	100	~ 130	25	20	6.7	0.07	200
Rai & Moin	0.1	1700	$250 \times 71 \times 361$	89	88	45	28	10.0	0.044	175
Case-Q1	2.5	1000	$258 \times 128 \times 130$	125	75	32	24.6	12.6	0.0057	143
Case-Q2	2.5	1000	$386 \times 128 \times 258$	125	75	32	16.2	6.2	0.0057	55

4 RESULTS

4.1 Mean Flow

In this section distributions of the mean quantities is presented. Temporal behavior of variables is assumed to be statistically stationary and homogeneity in the two horizontal spatial directions is taken into consideration throughout the analysis. The Reynolds-averaging was used in the calculation of mean-flow quantities and other higher-order turbulence statistics, requiring ensemble averages in time and also in each of the homogeneous directions x, and z. Denoting any flow quantity by ϕ, this operation can be written as:

$$\overline{\phi}(y) = \frac{1}{\Gamma L_x L_z} \int_0^{\Gamma} \int_0^{L_x} \int_0^{L_z} \phi(x,y,z,t)\, dz\, dx\, dt. \tag{21}$$

where Γ is the time interval over which the averaging is performed. The separation of instantaneous quantities into mean and fluctuation parts are generally done through Reynolds decomposition. Within the assumptions adopted in this work this decomposition can be expressed as:

$$\phi(x,y,z,t) = \overline{\phi}(y) + \phi'(x,y,z,t), \tag{22}$$

Table 2: Inner-layer velocity and length scales in the present simulations compared with incompressible work. Incompressible results were compiled from the semi-empirical formulae given White (1974).

	M	Re_{δ_1}	$\frac{\delta}{\delta_1}$	$\frac{u_\tau}{U_\infty}$	$\frac{\delta_1}{L^+}$	$\frac{\delta}{L^+}$
Case-Q1	2.5	1000	2.25	0.0504	50.4	113
Case-Q2	2.5	1000	2.37	0.0499	49.9	118
	0	500	7.73	0.0477	24	185
	0	1000	7.73	0.0450	45	345
	0	1500	7.73	0.0435	65	500
	0	2000	7.73	0.0425	85	667

and by definition,

$$\overline{\phi'} = 0. \tag{23}$$

When presenting the mean flow data, inner layer velocity, u_τ, and length, L^+, scales are often used, especially in the analysis of near-wall behavior:

$$L^+ = \frac{\mu/\rho}{u_\tau}, \tag{24}$$

and u_τ is the friction velocity based on the average wall-shear stress, $\overline{\tau_w}$:

$$u_\tau = \sqrt{\frac{\overline{\tau_w}}{\rho}}. \tag{25}$$

The resulting nondimensional quantities are denoted by superscript $()^+$ following the usual convention. Reynolds decomposition (Eq. 22) is employed in the definition of such quantities expressed in wall units, for example:

$$u^+ = \frac{\overline{u}}{u_\tau}. \tag{26}$$

Table 2 compares the inner-layer scales with the incompressible values at comparable Reynolds numbers. The ratio of the boundary layer thickness to the viscous length scale, δ/L^+, is a measure of the relative size of the large-scale, outer-layer structures compared with the size of the small-scale, inner-layer motions and is generally accepted to be a strong function of the Reynolds number. The simple comparison provided by Table 2 shows that this ratio is a weaker function of the Mach number. The impetus of the present work is to reveal the effect of compressibility on the separation and the dynamical coupling between the scales.

The distributions of mean and base streamwise velocities in wall units are given in Figure 2. Very near the wall in the sublayer where $y^+ < 12$, satisfactory agreement with the expected linear distribution, $u^+ = y^+$, is obtained. In the outer layer where $y^+ > 100$, the mean flow deviates significantly from the base flow as the mean streamwise velocity profiles are devoid of a wake (entrainment) region. As discussed earlier, the base flow was obtained from the solutions of boundary-layer type equations. The assumptions of the present work do not permit boundary layer growth and entrainment. Therefore, the solution while keeping the correct behavior in the near-wall region, converges onto a solution consistent with the adopted assumptions.

The density and the temperature fields show a variation of 250% at $M = 2.5$. This introduces significant density stratification across the boundary layer thickness. Also, the Reynolds-mean dynamic viscosity shows a variation of 70% at $M = 2.5$ which would have seriously handicapped a constant viscosity assumption.

4.2 Fluctuation Fields

In this section, the behavior of fluctuating quantities is explained by using second-order, one-point correlations in the context of Reynolds decomposition of time-dependent variables. The r.m.s. quantities are computed as:

$$\phi_{rms} = \sqrt{\overline{\phi'\phi'}} \tag{27}$$

where ϕ denotes any flow variable. Primitive variables such as density, velocity and temperature are used to facilitate comparisons with compressible boundary layer experiments as well as incompressible boundary layer studies.

Figure 3 gives the r.m.s. values of the velocity fluctuations normalized by the friction velocity, u_τ, as a function of the distance from the wall in wall-units. Close to the wall, the strongest fluctuations take place in the streamwise velocity. Fluctuations in the wall-normal velocity decay most rapidly close to the wall among the three velocity components, whereas away from the wall, u^+_{rms} and w^+_{rms} fluctuations decay more rapidly than v^+_{rms}. This behavior of the r.m.s. quantities is in agreement with previous turbulent boundary layer studies. Figure 4 provides the comparison of the u^+_{rms} distributions with previous incompressible DNS of Spalart (1988), incompressible experiments of Klebanoff (1955), and supersonic turbulent boundary layer experiments of Kistler (1959). The distance from the wall is given in units of boundary layer thickness, δ, to avoid the necessity of estimating the inner-layer scales of the compressible experiments. In accordance with the simulations of Spalart (1988), δ is evaluated to be the distance from the wall at which $\overline{u}$ reaches 99.8% of its free-stream value, giving a good match with published values, for instance with Klebanoff (1955). The Reynolds number in the experiments are orders of magnitude larger than the computations, and the gap is especially wide in the compressible studies. It can be observed from the simulations of Spalart (1988) that the maximum of u^+_{rms} approaches the wall as its magnitude increases with the Reynolds number. Increasing the Mach number has an attenuating effect on the turbulence level as seen in the experiments of Kistler (1959). Consequently, both the compressibility and the low-Reynolds-number effects are strong in the present computations and act in the same direction, i.e. reduce the turbulent intensities. The mild bulge in the u^+_{rms} distributions around $0.2 < y/\delta < 0.8$ in Figure 4 is attributed to the mechanisms of streamwise boundary layer growth which is neglected in the present model because of the streamwise periodicity assumption. Figure 5 displays turbulent primary shear stress, $-(u'v')^+$, distributions. As typical of turbulent wall-shear layers, turbulent primary shear stress is positive definite throughout the domain. The low Reynolds number in the present computations combined with finite compressibility yields lower fluctuation levels as well as a weaker turbulent shear stress. Although the vigor of the fluctuations is much subdued in the low Reynolds numbers, the turbulence generation and sustenance mechanisms are relatively uneffected by the changes in the Reynolds number.

The basis of the Morkovin hypothesis (Morkovin 1962), Strong Reynolds Analogy (Bradshaw 1977), is based on the similarity of density and temper-

ature fluctuation fields to the velocity fluctuations,

$$\frac{\rho'}{\overline{\rho}} \approx \frac{T'}{\overline{T}} \approx (\gamma - 1)M^2 \frac{u'}{U_\infty}, \tag{28}$$

under the assumption that the pressure fluctuations are negligible, the velocity fluctuations are small, and the Mach number is not larger than 4 or 5 (hence no appreciable changes in the stagnation temperature) for boundary layer flows. Strong Reynolds Analogy implies that temperature and density fluctuations are caused by the transport of mean-temperature or mean-density fields by the velocity fluctuations. Total velocity fluctuations, q, is defined as:

$$q^2 = \frac{1}{2}\left(u'u' + v'v' + w'w'\right). \tag{29}$$

In the present simulations, the pressure fluctuations are several orders of magnitude smaller than the velocity fluctuations. The validity of the Strong Reynolds Analogy is checked directly in Figure 6. The density and temperature profiles coalesce as a consequence of almost uniform pressure field. The velocity fluctuations fall within 20% of the analogy given in Eq. (28).

4.3 Spectral Analysis

Instantaneous data volumes were expanded in a Fourier series in homogeneous directions x, and z as:

$$\phi(x, y, z, t) = \sum_{k_1} \sum_{k_2} \hat{\phi}(y, k_1, k_2, t)$$

$$\exp\left(ik_1 \frac{2\pi}{L_x} x + ik_2 \frac{2\pi}{L_z} z\right), \tag{30}$$

where $|k_1| < \frac{1}{2}N_x$, $|k_2| < \frac{1}{2}N_z$, N_x and N_z are the number of nodes in z and θ directions, respectively. The temporal behavior of the flow field and the Fourier coefficients is assumed to be statistically stationary, therefore, ensemble averages of the coefficients were taken over the sample data volumes which had been saved. The maximum amplitudes in the wall-normal direction are presented:

$$\boldsymbol{F}_\phi(k_1, k_2) = \frac{1}{\Gamma} \int_0^\Gamma \underset{y}{\text{maximum}} \quad [\hat{\phi}\hat{\phi}^*] dt. \tag{31}$$

where superscript, ()* denotes the complex conjugate operation, and Γ is the time interval over which the time averaging is performed.

In Figure 7, the logarithms of the Fourier amplitudes (maxima in the y direction) of total velocity perturbations (q^2 in Eq. 29) are plotted over the two-dimensional wavenumber space of (k_x, k_z) for two grid resolutions at which the simulations were performed. The (0,0) mode is suppressed to better relate the analysis to the turbulent (fluctuating) quantities. The spectra, $\boldsymbol{F}_{qq}$, reveal a smooth surface decaying from the lower to higher wavenumbers. It is shown that the amount of decay is directly related to the separation of scales in the turbulence and is strongly affected by low-Reynolds number effects. Consequently, higher resolution levels are required for simulating high Reynolds-number turbulence. In the present simulations, amplitude decay takes place over four decades from the largest scales to the smallest scales. The decay is observable in every section of the two-dimensional wavenumber space, convincingly indicating that the scales contained in the present direct simulations are properly resolved. The dissipation end of the spectra, corresponding to high k_x and k_z is devoid of any corrugations and does not present any aliasing errors.

Details of the information from the Fourier analysis can be obtained by studying the one-dimensional spectra. Essentially, the one-dimensional Fourier analysis is equivalent to taking a section of the two-dimensional Fourier space along the zeroth (mean) wavenumber in the other direction. In this way, Figure 8 displays one-dimensional Fourier spectrum as a function of k_x or k_z on the log-log plots. Again, the zeroth mode is not included in these plots. In general, the spectra tend to be smoother in the spanwise direction than the streamwise. This general behavior was also observed by Spalart (1988) in his simulations of incompressible boundary layers. The streamwise velocity spectrum, $\boldsymbol{F}_{qq}$ reveals about seven decades of decay in k_x and six decades in k_z. The spectrum, $\boldsymbol{F}_{qq}$ exhibits an inertial subrange which is tangent to the $-5/3$ curve for about a decade. However short, this inertial subrange indicates the separation of scales in the streamwise direction. On the other hand, no inertial subrange behavior is observable from the k_z-spectra. As it was concluded in the incompressible simulations of Spalart (1988), much higher Reynolds numbers are required to see the development of an inertial range in the spanwise direction.

4.4 Two-Point Correlations

In the present problem, the turbulent flow field is assumed to be statistically stationary (or quasi-steady), therefore, time-averaging is appropriate for the collection of statistical measures such as the correlation tensor, so that the averaged quantities are functions of the spatial coordinates. The turbulent field variables used in this section are defined to be the fluctuating parts as defined by the conventional Reynolds-decomposition (Eq. 22). When a spatial direction is assumed homogeneous, it is more appropriate to describe spatial separations than separate locations and to perform ensemble-averaging in that direction. The present turbulent flow field is homogeneous in the x and z directions and the formulation now becomes:

$$\boldsymbol{Q}_{\phi,\theta}(\Delta x, \Delta z, y_a, y_b) = \frac{1}{\Gamma}\frac{1}{L_x}\frac{1}{L_z}\int_0^{\Gamma}\int_0^{L_x}\int_0^{L_z} \phi(x, y_a, z)\ \theta(x + \Delta x, y_b, z + \Delta z)\ dz\ dx\ dt \tag{32}$$

where $-L_x/2 < \Delta x < +L_x/2$ and $-L_z/2 < \Delta z < +L_z/2$ are the separations considered in the streamwise and the spanwise directions respectively and a and b denote two spatial locations in the flow field. The above defined double correlation function is generally normalized by the root-mean-square quantities to be presented as the correlation coefficient:

$$\boldsymbol{R}_{\phi,\theta}(\Delta x, \Delta z, y_a, y_b) = \frac{\boldsymbol{Q}_{\phi,\theta}(\Delta x, \Delta z, y_a, y_b)}{\sqrt{\overline{\phi^2(y_a)}}\ \sqrt{\overline{\theta^2(y_b)}}} \tag{33}$$

For no-separation case, $\Delta x = \Delta z = y_a - y_b = 0$, one-point correlation definition is directly recovered from the double correlation definitions.

$$\boldsymbol{Q}_{\phi,\theta}(\Delta x = 0, \Delta z = 0, y_a, y_a) = \overline{\phi\theta}(y_a) \tag{34}$$

Figure 9 compares the two-point correlations in the $(\Delta x^+, \Delta z^+)$ plane with one (computational) probe fixed at different $y_a^+ = y_b^+$ locations. These distributions could be best interpreted as the horizontal cross-sections of a typical event in the boundary layer. Smits et al. (1989) showed in their experiments that large scale structures in the outer region are broader in the spanwise direction for subsonic turbulent boundary layers than supersonic boundary layers. The present work extends the validity of this conclusion into the inner layer confirming the speculations of these authors.

The striking change of sign in $-\boldsymbol{R}_{uv}$ with spanwise separation (Δz^+) implies a high degree of organization of the large-scale eddies similar to in the incompressible turbulent wall-shear layers (Kovasznay 1970). This consistent behavior is the result of large eddies having a characteristic (or preferred) structure and an orientation. According to Figure 9, positive Reynolds-shear-stress contributions are accompanied by negative contributions in their neighborhood. The strength of this negative region decreases with y_a^+. Incompressible studies (Kim, Moin & Moser 1987, Head & Bandyopadhyay 1981) showed that during a typical burst event in the near-wall region, the low-momentum fluid is carried away from the wall region producing positive Reynolds-shear-stress. Complementing the strong bursts (on a statistically average sense), high-momentum fluid is slowed down and brought to the near-wall region by a weak sweep event with negative contributions to $-\boldsymbol{R}_{uv}$. Robinson (1990) gives an extensive account of possible events in the wall-shear layers, yielding the positive or negative contributions to the Reynolds stresses. The organization of such events is the key to reveal the dynamical coupling between inner and outer regions. The present work echoes the same argument for the compressible wall-shear layers at the supersonic velocities. Moreover, very strong similarity of the statistical distributions in the inner and outer parts of the turbulent boundary layer is observed instead of an abrupt or even a gradual change. Consequently, the events and structures are not confined to the near-wall region, they also extend or correlate with the outer layer.

The spanwise extents of all correlations increase considerably with the distance from the wall (Figure 9). This behavior is also clearly documented in the high-Reynolds number supersonic turbulent boundary layer experiments of Smits et al. (1989) and Spina et al. (1991) may indicate a general increase in the size of the structures in the wall-normal direction in accordance with the mixing-length or Townsend's "attached eddy" hypotheses. In the present work, it is shown that the correlation distributions actually contract in the streamwise direction with the wall-normal distance, very visibly in the $\boldsymbol{R}_{vv}$, $\boldsymbol{R}_{ww}$, and $-\boldsymbol{R}_{uv}$ correlations and to a lesser degree in $\boldsymbol{R}_{uu}$. These observations present strong evidence that turbulent events in the inner and outer layers are structurally connected, i.e. they are different stages in the evolution of a single structure. One mechanism in the evolution of these events is turbulence mixing which causes spreading in the spanwise direction. The momentum-redistribution mechanisms are also plausible because

the spreading rates of different velocity components are different. However, some other mechanism should also be present to cause the effect that seems to be a streamwise contraction.

Figure 10 compares the two-point correlations in $(\Delta x^+, y_a^+)$ plane by fixing one probe at different y_b^+ locations. $\boldsymbol{R}_{uu}$ distributions are not symmetric around the zero-streamwise-separation line, $\Delta x^+ = 0$, but have an inclination toward positive separations. The same phenomenon was also shown in the space-time isocorrelation distributions in the high-Reynolds number experiments of Robinson (1986) and Spina et al. (1991) at $M = 3$. Despite the one order of difference in the Reynolds numbers, the resemblance of the present results in Figure 10 with the experimental results is very striking and indicates that the basic structures of turbulence is relatively free from Reynolds number effects. The dashed lines shown in the contours of $\boldsymbol{R}_{uu}$ are the loci of the streamwise separation at maximum correlation close to the wall ($y^+ = 5.98$). Away from the wall, the angle of inclination increases, and the structure eventually aligns with the vertical at large distances from the wall. Another interesting phenomenon is the change in the angle of inclination around $\Delta x^+ = 0$. Such increasing tilt angle of the structures with the wall-normal distance is seen in the subsonic flows. However, the change in the tilt-angles in Figure 10 is dramatically sudden. The same rather sudden change in the inclination angles was also noted in the isocontours of $\boldsymbol{R}_{uu}$ by Robinson (1986) in the experiments with $M = 3.0$ turbulent boundary layer.

The tilting mechanism can also be observed from the increasing asymmetry of the $\boldsymbol{R}_{vv}$, $\boldsymbol{R}_{ww}$, and $-\boldsymbol{R}_{uv}$ around $\Delta x^+ = 0$ line. Sudden shift of the tilt angle is also evident in the contours of $\boldsymbol{R}_{vv}$, $\boldsymbol{R}_{ww}$, and $-\boldsymbol{R}_{uv}$. Negative regions seen in the $(\Delta z^+, y_a^+)$ plane in the $\boldsymbol{R}_{ww}$ correlations are observed to occur for the positive streamwise separations below the core of the structure and at the negative separations above it. The vertical length scale increases away from the wall but the streamwise length scale seems to decrease because of the change in the orientation of the structures.

4.5 Reynolds-Stress Budgets

For compressible flows, Favre (1965) introduced a variation of the Reynolds decomposition which incorporates the effect of variable density through mass-

weighted variables:

$$\phi(x,y,z,t) = \tilde{\phi}(y) + \phi''(x,y,z,t), \tag{35}$$

where $\tilde{\phi}$ is the Favre-mean of the quantity ϕ:

$$\tilde{\phi}(y) = \frac{\overline{\rho(x,y,z,t)\phi(x,y,z,t)}}{\overline{\rho}(y)} \tag{36}$$

In general, for turbulent flows with density stratification or fluctuations, the average of the Favre-fluctuation fields does not vanish while mass-weighted average does:

$$\overline{\phi''(x,y,z,t)} \neq 0, \tag{37}$$

$$\overline{\rho(x,y,z,t)\phi''(x,y,z,t)} = 0. \tag{38}$$

Using Favre decomposition reduces the complexity of the Reynolds-stress budget equations of compressible flows considerably (Rubesin & Rose 1973):

$$\frac{\partial}{\partial t}\left(\overline{\rho u_i'' u_k''}\right) + \frac{\partial}{\partial x_j}\left(\tilde{u}_j \overline{\rho u_i'' u_k''}\right) =$$

$$\boldsymbol{P}_{ik} + \boldsymbol{\Phi}_{ik} + \boldsymbol{\Theta}_{ik} + \boldsymbol{T}_{ik} + \boldsymbol{D}_{ik} - \boldsymbol{\epsilon}_{ik}. \tag{39}$$

Using the inner variables, u_τ and ν/u_τ, as velocity and length scales, the terms in Eq. (39) are given as:

$$\boldsymbol{P}_{ik} = -\overline{\rho u_k'' u_j''}\frac{\partial \tilde{u}_i}{\partial x_j} - \overline{\rho u_i'' u_j''}\frac{\partial \tilde{u}_k}{\partial x_j} \tag{40}$$

$$\boldsymbol{T}_{ik} = -\frac{\partial}{\partial x_j}\left(\overline{\rho u_i'' u_j'' u_k''}\right) \tag{41}$$

$$\boldsymbol{\Phi}_{ik} = \overline{p\left(\frac{\partial u_k''}{\partial x_i} + \frac{\partial u_i''}{\partial x_k}\right)} \tag{42}$$

$$\boldsymbol{\Theta}_{ik} = -\frac{\partial}{\partial x_i}\left(\overline{u_k'' p}\right) - \frac{\partial}{\partial x_k}\left(\overline{u_i'' p}\right) \tag{43}$$

$$\boldsymbol{D}_{ik} = -\frac{\partial}{\partial x_j}\left(\overline{u_k'' \tau_{ij}}\right) - \frac{\partial}{\partial x_j}\left(\overline{u_i'' \tau_{kj}}\right) \tag{44}$$

$$\boldsymbol{\epsilon}_{ik} = \overline{\tau_{ij}\frac{\partial u_k''}{\partial x_j}} + \overline{\tau_{kj}\frac{\partial u_i''}{\partial x_j}} \tag{45}$$

where $\boldsymbol{P}_{ik}$, $\boldsymbol{T}_{ik}$, $\boldsymbol{\Phi}_{ik}$, $\boldsymbol{\Theta}_{ik}$, $\boldsymbol{D}_{ik}$, $\boldsymbol{\epsilon}_{ik}$ denote the production, turbulent transport, pressure-strain, pressure-diffusion, viscous diffusion, and dissipation, respectively. It should be noted that the decomposition of the pressure and density into their mean and fluctuating parts is avoided in the present formulations. The customary $()^+$ notation is omitted from the flow variables which are expressed in wall units in this section. The notation will be kept for y^+ as a reminder that the wall-units are being used throughout.

For a statistically steady turbulent state, the sources and sinks appearing on the right-hand-side of the budget equation essentially should balance. In Reynolds-stress closure models, all high-order statistics which represent the sources and sinks of Reynolds stresses are modeled and the equations presented in Eq. (39) are solved coupled with the mean-momentum equations. The pressure-strain term is usually modeled directly whereas the pressure-diffusion term typically is treated together with the turbulent diffusion term. Also, the pressure-strain and pressure-diffusion terms are added together resulting in the pressure-gradient/velocity correlation, $\boldsymbol{\Pi}_{ij}$:

$$\boldsymbol{\Pi}_{ij} = \boldsymbol{\Phi}_{ij} + \boldsymbol{\Theta}_{ij} = -\overline{\frac{\partial p}{\partial x_i} u_j''} - \overline{\frac{\partial p}{\partial x_j} u_i''} \tag{46}$$

It is conjectured that the modeling of this compound term is physically not plausible as suggested by recent DNS analyses of incompressible turbulent flows (Mansour, Kim & Moin 1988, Huser & Biringen 1993) since $\boldsymbol{\Phi}_{ij}$ and $\boldsymbol{\Theta}_{ij}$ assume opposite-values as $\boldsymbol{\Pi}_{ij}$ approaches to zero near the wall.

To estimate the correct behavior of sources and sinks in the budget equations is a formidable task, especially in the near-wall region where all the terms are of comparable importance and the homogeneous turbulence assumptions do not hold. In the present work, all terms in the Reynolds-stress budgets are obtained directly from the present simulations. Hence, the critical assessment of model assumptions is done explicitly.

Within the horizontal periodicity approximation of the present mathematical model, the streamwise and spanwise derivatives of the ensemble-averaged quantities, as well as the wall-normal and spanwise Favre- or Reynolds-mean velocities vanish, such that,:

$$\frac{\partial \overline{\phi}}{\partial x} = \frac{\partial \overline{\phi}}{\partial z} = 0, \tag{47}$$

$$\frac{\partial \widetilde{\phi}}{\partial x} = \frac{\partial \widetilde{\phi}}{\partial z} = 0, \tag{48}$$

$$\overline{v} = \widetilde{v} = 0, \tag{49}$$

$$\overline{w} = \widetilde{w} = 0. \tag{50}$$

where ϕ denotes any fluctuating flow variable or quantity. These simplifications are reflected onto the analyses of the individual budgets of four non-zero Reynolds-stress components and the turbulent kinetic energy presented in Figure 11 after ensemble-averaging in time and in the homogeneous streamwise and spanwise directions. The results for lower grid-resolution case (**Case-Q1**) are presented in the following sections.

4.5.1 $\overline{\rho u''^2}$ Budget

Figure 11a gives the contributing terms to $\overline{\rho u''^2}$ budget. The budget is balanced to zero within 15% and the imbalance can be attributed to limited sampling size and numerical truncation errors. The terms slowest to converge are suspected to be the turbulent-diffusion terms since they are fourth-order statistical moments (in incompressible flow they would be only third order); pressure-gradient/velocity terms are also very slow to converge. The magnitude of these terms are very small in the original non-dimensionalization used in the computations, and significant precision is lost during rescaling with the wall units.

The details of the near-wall behavior for $M = 2.5$ agree well with the incompressible boundary layer DNS results of Spalart (1988). The largest positive contribution to the budget is from the production terms corresponding to the generation of turbulence through mean-flow gradients. The production reaches a peak at $y^+ \approx 20$ and is balanced mainly by the dissipation. The loss of turbulent energy by dissipation is maximum at the wall and decreases toward the outer layer. The local maximum in the dissipation loss coincides with the maximum production indicating the close local coupling between the two mechanisms in this equilibrium boundary layer. Viscous diffusion is positive near the wall and becomes negative for $y^+ > 10$ with a local minimum in the maximum production region showing that the turbulent energy produced is quickly diffused away. Turbulent diffusion on the other hand, is zero at the wall, becomes positive and then negative with an inflexion point at the maximum production area. The turbulence is carried

away from the high production areas toward the high-speed flow, but is actually enhanced toward the wall by turbulent diffusion. For this particular Reynolds-stress component, the pressure-diffusion is identically zero, consequently, $\boldsymbol{\Pi}_{11} = \boldsymbol{\Phi}_{11}$. Pressure-gradient-velocity terms are of small magnitude but clearly negative throughout the domain.

The magnitudes of the terms in the $\overline{\rho u''^2}$ budget equation are almost an order of magnitude lower than incompressible DNS results of (Spalart 1988). There is also a scale discrepancy in the wall-normal direction, for example, the maximum of the turbulent production in incompressible channel (Mansour et al. 1988) and boundary layer (Spalart 1988) simulations appears at about $y^+ = 15$ compared with $y^+ = 20$ in the present compressible simulations. These differences can be attributed to compressibility effects or to the smaller Reynolds numbers used in the present simulations. Nevertheless, the distributions are quite similar and the arguments in their interpretation remain valid with finite compressibility leading to the conclusion that compressibility effects attenuate the turbulence mechanisms without changing the basic dynamics.

4.5.2 $\overline{\rho v''^2}$ Budget

The contributions to $\overline{\rho v''^2}$ budget are shown in Figure 11b. This budget contains no direct contribution from production terms and the major source of energy is the pressure-gradient/velocity terms, $\boldsymbol{\Pi}_{22}$. The loss in the $\overline{\rho u''^2}$ budget through $\boldsymbol{\Pi}_{11}$ is redistributed by $\boldsymbol{\Pi}_{22}$ and $\boldsymbol{\Pi}_{33}$ into the $\overline{\rho v''^2}$ and $\overline{\rho w''^2}$ budgets. The pressure-strain term is also widely referred as redistribution or return-to-isotropy terms (Rotta 1951, Lumley & Newman 1977).

Figure 11b depicts $\boldsymbol{\Pi}_{22}$ as the sum of $\boldsymbol{\Phi}_{22}$ and $\boldsymbol{\Theta}_{22}$ terms and Figure 12a displays the pressure-strain and pressure-diffusion terms separately. As found in the incompressible channel simulations of Mansour et al. (1988) incompressible square-duct simulations of Huser & Biringen (1993), $\boldsymbol{\Phi}_{ij}$ and $\boldsymbol{\Theta}_{ij}$ assume very large magnitudes compared with the other terms of the balance equation, but have opposite signs. Modeling two such large terms separately may obscure the contribution from the other turbulent mechanisms and also may misrepresent the true partition of the turbulent kinetic energy.

The positive contributions through $\boldsymbol{\Pi}_{22}$ quickly attenuates close to the wall and very close to the wall where $y^+ < 20$, $\boldsymbol{\Pi}_{22}$ changes the sign representing a loss of energy from this budget. This wall effect is seen in the

incompressible turbulent wall-shear flow simulations of Mansour et al. (1988), Spalart (1988) and Huser & Biringen (1993), and referred to as the "splatting" effect. Turbulent transport is ineffective in the region of "splatting", and is positive when $\boldsymbol{\Pi}_{22}$ is not substantial and negative when it is. Viscous diffusion is positive close to the wall and negative for $y^+ > 40$. Dissipation loss is the substantial sink for this budget, increasing from zero at the wall to a maximum around $y^+ = 70$.

4.5.3 $\overline{\rho w''^2}$ Budget

Figure 11c displays the distributions of all contributing terms in $\overline{\rho w''^2}$ budget. As in the $\overline{\rho v''^2}$ equation, there is no direct contribution from the production term to this budget and the main energy source is the pressure-gradient/velocity term, $\boldsymbol{\Pi}_{33}$ receiving energy via the $\boldsymbol{\Pi}_{11}$ term. The pressure-diffusion for this budget balance is zero, and consequently, $\boldsymbol{\Pi}_{33} = \boldsymbol{\Phi}_{33}$ and the maximum in the pressure-strain term occurs at around $y^+ = 30$. The only appreciable sink in the budget is the dissipation which locally balances turbulent kinetic energy supplied by the pressure-strain terms. Close to the wall, for $y^+ < 30$, viscous diffusion is positive and is the dominant source term for $y^+ < 5$. The dissipation reaches a local minimum and increases rapidly towards the wall to dissipate the energy transported by the viscous mechanisms. Turbulent transport remains negligible throughout the domain.

4.5.4 Primary Reynolds-Shear-Stress Budget

The accurate prediction of the primary shear stress is very crucial because turbulence production takes place by the interaction of the mean velocity gradients with the primary shear stress (Hinze 1975). Any errors in the prediction (or modeling) of primary turbulent shear stress will be magnified in the mean streamwise momentum equation resulting in a less than accurate mean velocity profile and subsequent poor estimates of the quantities of practical concern such as the drag.

The balance of $-\overline{\rho u''v''}$ shown in Figure 11d includes a production term, a pressure-diffusion term and a pressure-strain term. As in the $\overline{\rho v''^2}$ budget, the pressure-diffusion and pressure-strain terms are almost identical but of opposite signs and each is two orders of magnitude larger than the other budget terms (Figure 12b). The production terms supply energy to the

budget with a broad maximum region for $20 < y^+ < 70$. Conspicuously different from the normal Reynolds-stress budgets, the main energy sink in the $-\boldsymbol{R}_{uv}$ budget is the pressure-gradient/velocity terms. Dissipation is effective only for $y^+ < 30$ mainly balancing the energy transported in by viscous diffusion mechanism. Turbulent transport is small but positive close to the wall ($y^+ < 30$) and is negative further away.

4.5.5 Turbulent Kinetic Energy Budget

The turbulent kinetic energy ($\boldsymbol{TKE}$) is defined as:

$$\boldsymbol{TKE} = \frac{\overline{\rho u_i'' u_i''}}{2} = \frac{1}{2}\left(\overline{\rho u''^2} + \overline{\rho v''^2} + \overline{\rho w''^2}\right). \tag{51}$$

For the present flow field the conservation equation for $\boldsymbol{TKE}$ is obtained as the trace of Eq. (39). The source of production of $\boldsymbol{TKE}$ is the interaction between the mean flow velocity gradient and the primary turbulent shear stress.

Figure 11e displays the near-wall distributions of the terms in the budget and because of the strong similarity in the budget, the discussion offered for the $\overline{\rho u''^2}$ budget is valid for the $\boldsymbol{TKE}$ budget except for the pressure-gradient/velocity. The pressure-strain term does not exist in the incompressible $\boldsymbol{TKE}$ budget equations since the fluctuation and the ensemble-mean velocity field is solenoidal for $M = 0$:

$$\frac{\partial u_i''}{\partial x_i} = 0. \tag{52}$$

Consequently, the $\boldsymbol{TKE}$ budget for the incompressible turbulent boundary layers include small, positive pressure-diffusion contributions near the wall for $y^+ < 15$ (Spalart 1988). For the compressible turbulent boundary layer considered here, the pressure-gradient/velocity term, $\boldsymbol{\Pi} = \boldsymbol{\Phi} + \boldsymbol{\Theta}$, (Figure 11e) is small, finite, and negative. Figure 12c shows the partition of $\boldsymbol{\Pi}$ between $\boldsymbol{\Phi}$ and $\boldsymbol{\Theta}$. As in the $\overline{\rho v''^2}$ and $-\overline{\rho u'' v''}$ budgets, $\boldsymbol{\Theta}$ and $\boldsymbol{\Phi}$ are of almost equal magnitudes, but of opposite signs. The non-zero pressure-strain term is an effect of compressibility and directly interferes with the partition of the energy between the momentum components in the near-wall region.

The pressure-gradient/velocity terms are responsible for the transfer of the turbulent energy generated in the $\overline{\rho u''^2}$ budget to the $\overline{\rho v''^2}$ and $\overline{\rho w''^2}$

budgets as shown in the previous sections:

$$\boldsymbol{\Pi}_{11} \rightarrow -\boldsymbol{\Pi}_{22} - \boldsymbol{\Pi}_{33}. \tag{53}$$

In incompressible flows, this transfer takes place in a state of local and instantaneous balance, i.e. the turbulent energy generated at one location will be instantaneously distributed between the momentum components. Therefore, the energy transfer depicted in Eq. (53) is an equality at all times and at all spatial locations. Pressure, which is a kinematic quantity in incompressible flows, provides the necessary communication between the momentum components. There should be no spatial or temporal delay in this mechanism since the sound speed, the speed at which the information is passed through the fluid medium, is infinite and the velocity field is always solenoidal.

In compressible turbulent boundary layer flows considered here, the local (and instantaneous) balance of pressure-velocity interactions does not seem to hold. For compressible flows, pressure is a thermodynamic quantity and the sound speed is finite. Consequently, information transfer from point to point takes place with a certain spatial and temporal delay through the fluid medium. The orientations of the turbulence generating events could certainly effect the communication between the momentum components. It is then possible that a locally non-zero pressure-strain term is accommodated in the $\boldsymbol{TKE}$ budget. At the relatively low Mach number of the present simulations, this effect is revealed only in the small, non-zero pressure-strain distribution in the $\boldsymbol{TKE}$ budget. This effect should be accentuated with increasing Mach numbers where it contributes substantially to the $\boldsymbol{TKE}$ budget.

4.6 Modeling pressure-gradient velocity correlations

In this section, a recently proposed turbulence model (Speziale & Sarkar 1991) for the pressure gradient-velocity correlation, $\boldsymbol{\Pi}_{ij}$, is tested and evaluated using the data base from the present direct numerical simulations. It should be noted that experimentally these correlations are the most difficult to measure and therefore DNS data are the only source for assessment of closure models developed for these terms. In second-order closure modeling, the deviatoric (zero-trace) part of $\boldsymbol{\Pi}_{ij}$ appears in the Reynolds-stress transport equations:

$$\boldsymbol{\Pi}^{d}_{ij} = \overline{u'_i \frac{\partial p'}{\partial x_j}} + \overline{u'_j \frac{\partial p'}{\partial x_i}} - \frac{2}{3}\overline{u'_i \frac{\partial p'}{\partial x_j}}. \tag{54}$$

Speziale & Sarkar (1991) assumed that the main compressibility effects are through changes in mean density, and used a variable density extension of the SSG model originally derived by Speziale, Sarkar & Gatski (1991) for incompressible turbulent flows:

$$\begin{aligned}\boldsymbol{\Pi}_{ij}^{d} = \quad & \overline{\rho}\left[(C_1\epsilon + C_1^* P)\, b_{ij}\right. \\ & -C_2\epsilon\left(b_{ik}b_{kj} - \frac{1}{3}II\delta_{ij}\right) \\ & -C_3 K\left(b_{ik}\widetilde{S}_{jk} + b_{jk}\widetilde{S}_{ik} - \frac{2}{3}b_{mn}\widetilde{S}_{mn}\delta_{ij}\right) \\ & -C_4 K\left(b_{ik}\widetilde{W}_{jk} + b_{jk}\widetilde{W}_{ik}\delta_{ij}\right) \\ & \left.-\frac{4}{5}\left(1 - C^* II^{\frac{1}{2}}\right)\left(\widetilde{S}_{ij} - \frac{1}{3}\widetilde{S}_{kk}\delta_{ij}\right)\right] \end{aligned} \tag{55}$$

where

$$b_{ij} = \frac{\left(R_{ij} - \frac{2}{3}K\delta_{ij}\right)}{2K}, \tag{56}$$

$$II = b_{ij}b_{ij}, \tag{57}$$

$$\widetilde{S}_{ij} = \frac{1}{2}\left(\frac{\partial \widetilde{u}_i}{\partial x_j} + \frac{\partial \widetilde{u}_j}{\partial x_i}\right), \tag{58}$$

$$\widetilde{W}_{ij} = \frac{1}{2}\left(\frac{\partial \widetilde{u}_i}{\partial x_j} - \frac{\partial \widetilde{u}_j}{\partial x_i}\right), \tag{59}$$

$$R_{ij} = \frac{\overline{\rho u_i'' u_j''}}{\overline{\rho}}, \quad \epsilon = \frac{\overline{\tau_{ij}' \dfrac{\partial u_i'}{\partial x_j}}}{\overline{\rho}}, \tag{60}$$

$$K = \frac{1}{2}R_{ii}, \quad P = -R_{ij}\frac{\partial \widetilde{u}_i}{\partial x_j}. \tag{61}$$

The dimensionless model constants were determined through invariance and consistency arguments and optimized for incompressible, homogeneous turbulent flows and are given as,

$$\begin{aligned} & C_1 = 3.4,\ C_1^* = 1.80,\ C_2 = 4.2, \\ & C_3 = 1.25,\ C_4 = 0.40,\ C^* = 1.62. \end{aligned} \tag{62}$$

For the present comparisons, the equations are expressed in wall-units. In boundary layer flows, pressure-velocity interactions are concentrated in the near wall region, $y^+ < 100$. The near-wall region is a highly anisotropic part of the field and it is recommended that wall functions should be employed for the proper representation of this anisotropy of ϵ (Speziale & Sarkar 1991). Therefore, in Eq. (55), a wall function, f is introduced to modify C_1 by $C_1 f$. The function f varies between 0 and 1 across the sublayer, $0 < y^+ < 100$, and is given as:

$$f = 1 - \exp\left(-\frac{y^+}{A^+}\right)^2 \tag{63}$$

where $A^+ = 80$ was used during the comparisons. Physically, the use of the wall function amounts to relaxing the homogeneity assumption where it is violated most severely, i.e. on the dissipation and production rates, ϵ and P respectively. In other words, it is the simplest way to patch the outer layer solution to the near wall region.

The mean flow quantities including the Reynolds stresses, R_{ij}, and the turbulent dissipation rate, ϵ, are explicitly obtained from the DNS data base to calculate the terms appearing on the right-hand-side of Eq. (55). The model prediction for $\boldsymbol{\Pi}^d$ is then compared with the DNS values obtained by constructing the pressure gradient-velocity correlations in Eq. (54) directly with no model assumptions.

Figure 13a presents the model prediction and the DNS construction for $\boldsymbol{\Pi}^d_{11}$ indicating that the magnitude and the behavior of the interaction term are properly captured by the model; the comparison is also satisfactory for $\boldsymbol{\Pi}^d_{22}$ (Figure 13b) but the model cannot properly capture the "splatting" effect which appears as a sign reversal in the very-near-wall-region. Similarly, Figure 13c offers a comparison for $\boldsymbol{\Pi}^d_{33}$, showing qualitative agreement between the DNS and the model. The comparison of the interaction terms in the turbulent shear stress transport equation is given in Figure 13d with significant distribution differences. The comparison at this proximity to the wall is actually quite satisfactory considering that the model utilizes the ideas from isotropic homogeneous turbulent flows. It should be noted that, in general turbulence models are developed for high-Reynolds number flows whereas the DNS studies such the present one suffer from low-Reynolds number effects; therefore these comparisons should be interpreted considering such differences.

4.7 Instantaneous Fields

In this section, the cross-sectional views of instantaneous flow fields are presented and analyzed. Perturbation quantities obtained from Reynolds decomposition of total quantities are used throughout the analysis. In all the contour and vector plots, the turbulent field variables and the coordinate directions are nondimensionalized by viscous wall scales (Equations 24 and 25) and are denoted by superscript $()^+$. For brevity, the customary notation $()'$ for the Reynolds-decomposed fluctuating quantities is not used. Since a qualitative understanding of the turbulent structures and flow topology is sought, the majority of results are given only for the lower resolution case. To offer a better representation of the structures, the figures are not drawn to scale.

Figure 14 presents the wall-normal perturbation velocity, v^+, contours in the horizontal (x^+, z^+) planes at different y^+ cross-sections. The upwelling motion of the fluid caused by the bursting events can be easily identified by the positive contours whereas the negative contours are associated with fluid motions towards the wall. The contours at $y^+ = 23$ indicate that the turbulent events actually protrude deep into the viscous sublayer. Short-length turbulent structures are followed by long regions of laminar flow at distances close to the wall. Away from the wall, the turbulent activity level increases and the turbulent structures occupy a large portion of the flow and longer positive contours in the streamwise direction indicates streakiness of the flow structures. At $y^+ = 113$ in Figure 14, the turbulence activity reaches its peak and for increasing y^+, the turbulence level decreases as the structures have shorter streamwise extent and lose their streaky appearance.

Figure 15 displays (w^+, v^+) velocity vectors in the cross-stream plane. The wall-normal extent of the plot is about one boundary layer thickness ($\delta^+ = 270$). In most of the instances, the upwelling motions are accompanied by decelerations, and the motions toward the wall are caused by accelerations in the streamwise velocity. Negative uv correlation acts as a positive Reynolds stress and regions of strong uv correlations correspond to regions where streamwise momentum is diffused away from the wall by turbulence. As the ejection extends away from the wall into the outer layer, it loses its strength and expands while there is an inrush of fluid which detaches the structure from the wall. the correlation between u^+ and v^+ is positive yielding locally negative Reynolds-shear stress. The upwelling and down-

ward motions interact in a intricate way. Strong bendings of either motion correspond to a strong perturbation vorticity in the cross-stream plane. The vortices generated with this or other mechanisms are subject to straining and diffusive effects in the flow field as well as pairing and de-pairing vortex interactions.

5 CONCLUSIONS

In this computational study, the effects of compressibility on the fully-developed turbulence were investigated. This equilibrium turbulent flow includes the anisotropy and inhomogeneity effects due to the existence of a solid boundary. In general, broad similarities are found between the incompressible and compressible turbulent boundary layers. However, significant differences exist due to the finite, supersonic Mach numbers of the present simulations. The overall effects of compressibility on turbulence are manifested through density gradients across the boundary layer, variable fluid properties, and the damping effect on turbulent motions. The dissipative mechanisms are enhanced in compressible flows which, in turn, result in less vigorous turbulence in the boundary layer.

The present work provides a documentation of the energy balances and the structural dynamics of compressible boundary layer turbulence. Quasi-periodic structures and events in the turbulent boundary layer and the turbulent energy balance are interdependent as the origin of structures are related to turbulence production and their breakup to dissipation. Such strong-burst and weak-sweep events have been previously identified in incompressible wall-shear layers, and their origin has been connected with hairpin vortices. In the present work, the large scale structures in supersonic boundary layers are found to be broader in the spanwise direction and with a greater angle of inclination toward the wall. Present computations revealed that these events penetrate deep into the viscous sublayer. With the distance from the wall, the inclination decreases and the structures assume up-right position in the outer layer. Between the upstream and downstream parts of an average structure, there is a sudden change of the inclination angle. Vertical scales of structures can be as large as 0.5δ, consequently, an average large scale motion spans almost the whole boundary layer. Therefore, at least for the low-Reynolds numbers of the present simulations, the dynamics of such

events may describe the whole boundary layer.

The turbulent energy balance is strongly similar to incompressible wall-shear layers: in the far field, the turbulent production balances dissipation and all contributing terms attain comparable magnitudes in the near-wall region. Compressibility effects are responsible for the lower magnitudes and non-zero values of the pressure-strain terms in the turbulent kinetic energy.

References

BIRINGEN, S. & SAATI, A. 1990, Comparison of several finite-difference methods, *Journal of Aircraft* **72**, 90–92.

BRADSHAW, P. 1977, Compressible turbulent shear layers, *Annual Review of Fluid Mechanics* **9**, 33–54.

COLES, D. 1964, The turbulent boundary layer in a compressible fluid, *Physics of Fluids* **7**, 1403–1423.

ERLEBACHER, G. & HUSSAINI, M. Y. 1989, Numerical experiments in supersonic boundary layer stability, *Physics of Fluids* **A 2**, 99–104.

ERLEBACHER, G., HUSSAINI, M. Y., KREISS, H. O. & SARKAR, S. 1990, The analysis and simulation of compressible turbulence, *Theoretical and Computational Fluid Dynamics* **2**, 73–95.

FAVRE, A. 1965, Equations des Gaz Turbulents Compressibles, *Journal de Mecanique* **4**, 361–390.

FEIEREISEN, W. J., REYNOLDS, W. C. & FERZIGER, J. H. 1981, Numerical simulation of a compressible homogeneous, turbulent shear flow, *Report* **TF-13**, Stanford University.

GOTTLIEB, D. & TURKEL, E. 1976, Dissipative two-four methods for time-dependent problems, *Mathematical Computation* **30**, 703.

HEAD, M. R. & BANDYOPADHYAY, P. 1981, New aspects of turbulent boundary-layer structure, *Journal of Fluid Mechanics* **107**, 297–338.

HINZE, J. O. 1975, *Turbulence*, McGraw-Hill, New York.

HUSER, A. & BIRINGEN, S. 1993, Direct numerical simulation of turbulent flow in a square duct, *Journal of Fluid Mechanics* **257**, 65–95.

KIM, J., MOIN, P. & MOSER, R. 1987, Turbulence statistics in fully developed channel flow at low Reynolds number, *Journal of Fluid Mechanics* **177**, 133.

KISTLER, A. L. 1959, Fluctuation measurements in a supersonic turbulent boundary layer, *Physics of Fluids* **2**, 290–296.

KLEBANOFF, P. S. 1955, Characteristics of turbulence in a boundary layer with zero pressure gradient, *Report* **1247**, NACA.

KOVASZNAY, L. S. G. 1970, The turbulent boundary layer, *Annual Review of Fluid Mechanics* **2**, 95–112.

LUMLEY, J. L. & NEWMAN, G. R. 1977, The return to isotropy of homogeneous flows, *Journal of Fluid Mechanics* **82**, 161–178.

MANSOUR, N. N., KIM, J. & MOIN, P. 1988, Reynolds-stress and dissipation-rate budgets in a turbulent channel flow, *Journal of Fluid Mechanics* **194**, 15–44.

MORKOVIN, M. V. 1962, Effects of compressibility on turbulent flows, *in* A. V. Favre (ed.), *Mechanique de la Turbulence*, Centre National de la Recherche Scientifique, Paris, France, p. 367.

PASSOT, T. & POUQUET, A. 1987, Numerical simulation of compressible homogeneous flows in the turbulent regime, *Journal of Fluid Mechanics* **181**, 441–466.

PORTER, D. H., POUQUET, A. & WOODWARD, P. R. 1992, Three-dimensional supersonic homogeneous turbulence: a numerical study, *Physical Review Letters* **68**(21), 3156–3159.

RAI, M. M. & MOIN, P. 1993, Direct numerical simulation of transition and turbulence in a spatially evolving boundary layer, *Journal of Computational Physics* **109**, 169–172.

ROBINSON, S. K. 1986, Space-time correlation measurements in a compressible turbulent boundary layer, *Paper* **86-1130**, AIAA.

ROBINSON, S. K. 1990, A perspective on coherent structures and conceptual models for turbulent boundary layer physics, *Paper* **90-1638**, AIAA.

ROTTA, J. 1951, Statistiche therorie nichthomegener Turbulenz, *Z. Phys* **129**, 547–572.

RUBESIN, M. W. & ROSE, W. C. 1973, The turbulent mean-flow, Reynolds-stress, and heat-flux equations in mass-averaged dependent variables, *Technical Momerandum* **X-62248**, NASA.

SARKAR, S., ERLEBACHER, G. & HUSSAINI, M. Y. 1991a, Direct simulation of compressible turbulence in a shear flow, *Theoretical and Computational Fluid Dynamics* **2**, 291–305.

SARKAR, S., ERLEBACHER, G., HUSSAINI, M. Y. & KREISS, H. O. 1991b, The analysis and modeling of dilatational terms in compressible turbulence, *Journal of Fluid Mechanics* **227**, 473–493.

SMITS, A. J., SPINA, E. F., ALVING, A. E., SMITH, R. W., FERNANDO, E. M. & DONOVAN, J. F. 1989, A comparison of the turbulence structure of subsonic and supersonic boundary layers, *Physics of Fluids* **A 1**(11), 1865–1875.

SPALART, P. R. 1988, Direct simulation of a turbulent boundary layer up to $Re_\theta = 1410$, *Journal of Fluid Mechanics* **187**, 61.

SPEZIALE, C. G. & SARKAR, S. 1991, Second-order closure models for supersonic turbulent flows, *Paper* **91-0217**, AIAA.

SPEZIALE, C. G., SARKAR, S. & GATSKI, T. N. 1991, Modelling the pressure-strain correlation of turbulence: an invariant dynamical systems approach, *Journal of Fluid Mechanics* **227**, 245–272.

SPINA, E. F., DONOVAN, J. F. & SMITS, A. J. 1991, On the structure of high-Reynolds number supersonic turbulent boundary layers, *Journal of Fluid Mechanics* **222**, 293–327.

SPINA, E. F. & SMITS, A. J. 1987, The effect of compressibility on the large-scale structure of a turbulent boundary layer, *Paper* **87-0195**, AIAA.

WHITE, F. M. 1974, *Viscous Fluid Flow*, McGraw-Hill, New-York.

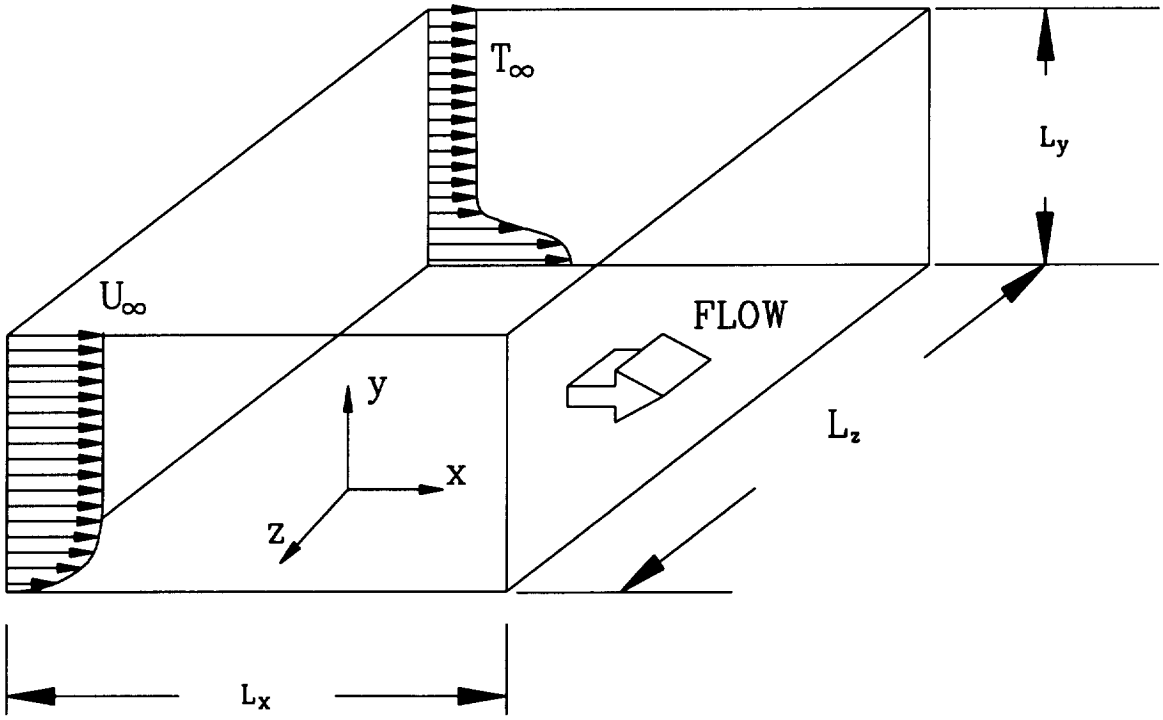

Figure 1: Geometry and coordinate system for compressible boundary layer over a flat plate.

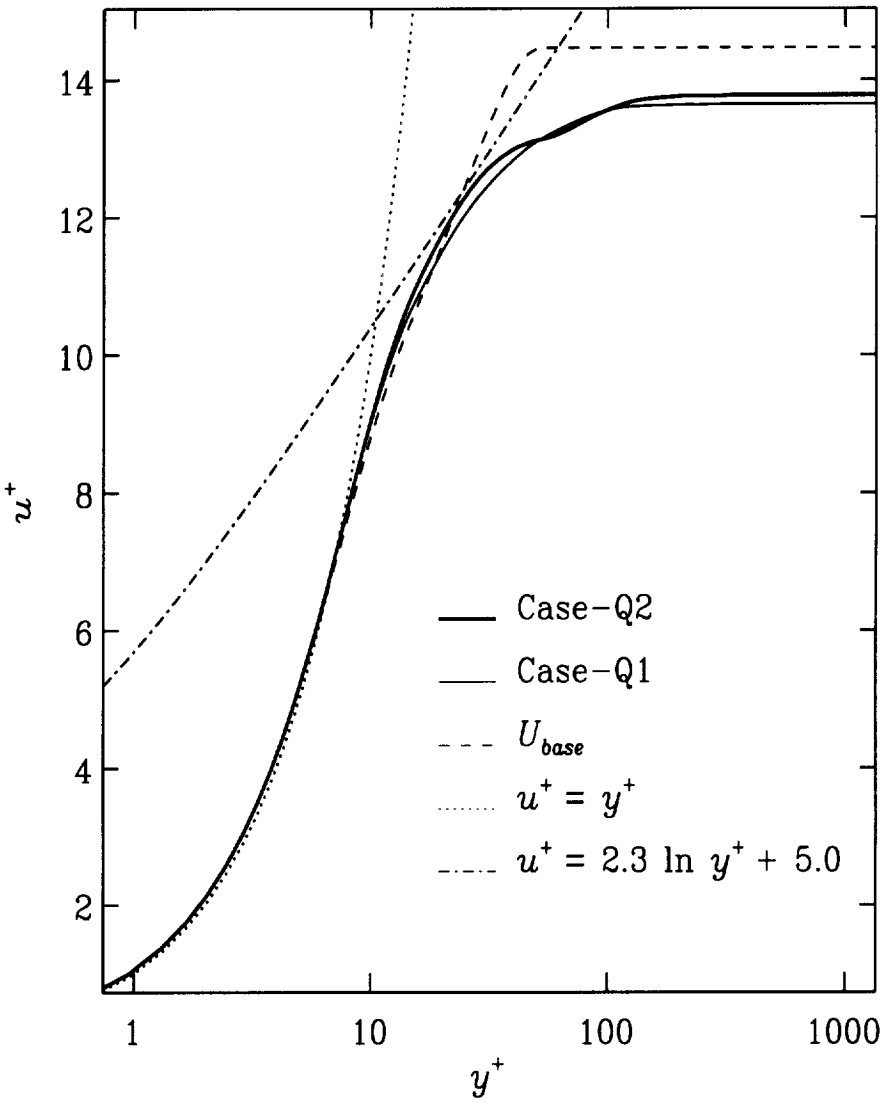

Figure 2: Comparison of the mean flow with the base flow and the inspection of the near-wall behavior.

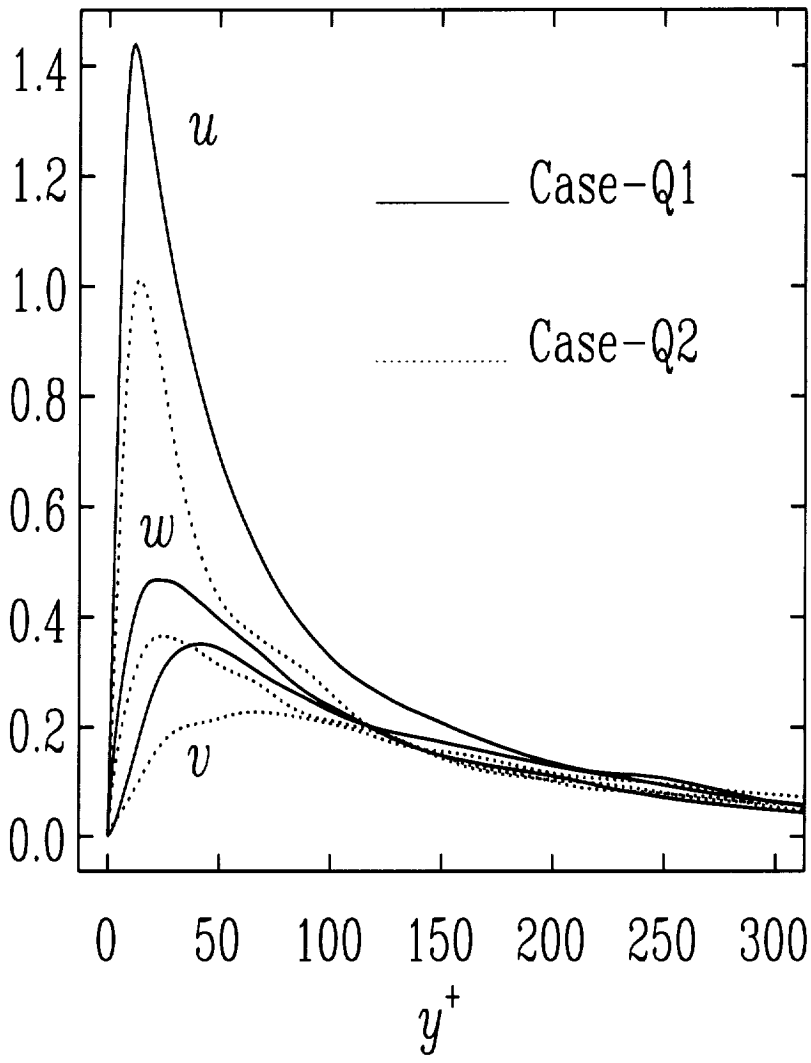

Figure 3: Velocity fluctuation levels in wall-units.

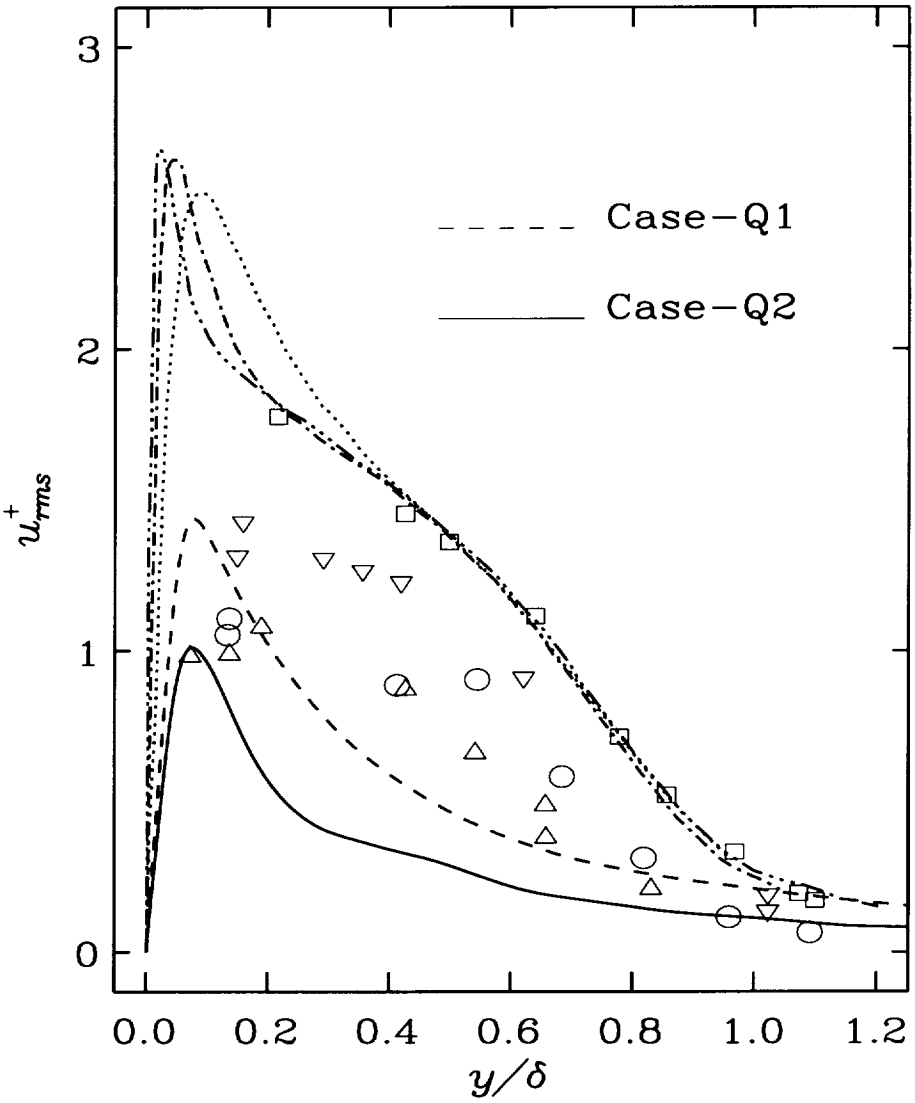

Figure 4: Comparison of u^+_{rms} distributions with experiments and incompressible computations. ····· , $M = 0, Re_{\delta_1} = 500$ (Spalart 1988); — · — , $M = 0, Re_{\delta_1} = 1500$ (Spalart 1988); — ··· —, $M = 0, Re_{\delta_1} = 2000$ (Spalart 1988); □, $M = 0, Re_{\delta_1} = 12,000$ (Klebanoff 1955); ▽, $M = 1.72, Re_{\delta_1} = 2 \times 10^5$ (Kistler 1959); ○, $M = 3.56, Re_{\delta_1} = 2 \times 10^5$ (Kistler 1959); △, $M = 4.67, Re_{\delta_1} = 2 \times 10^5$ (Kistler 1959).

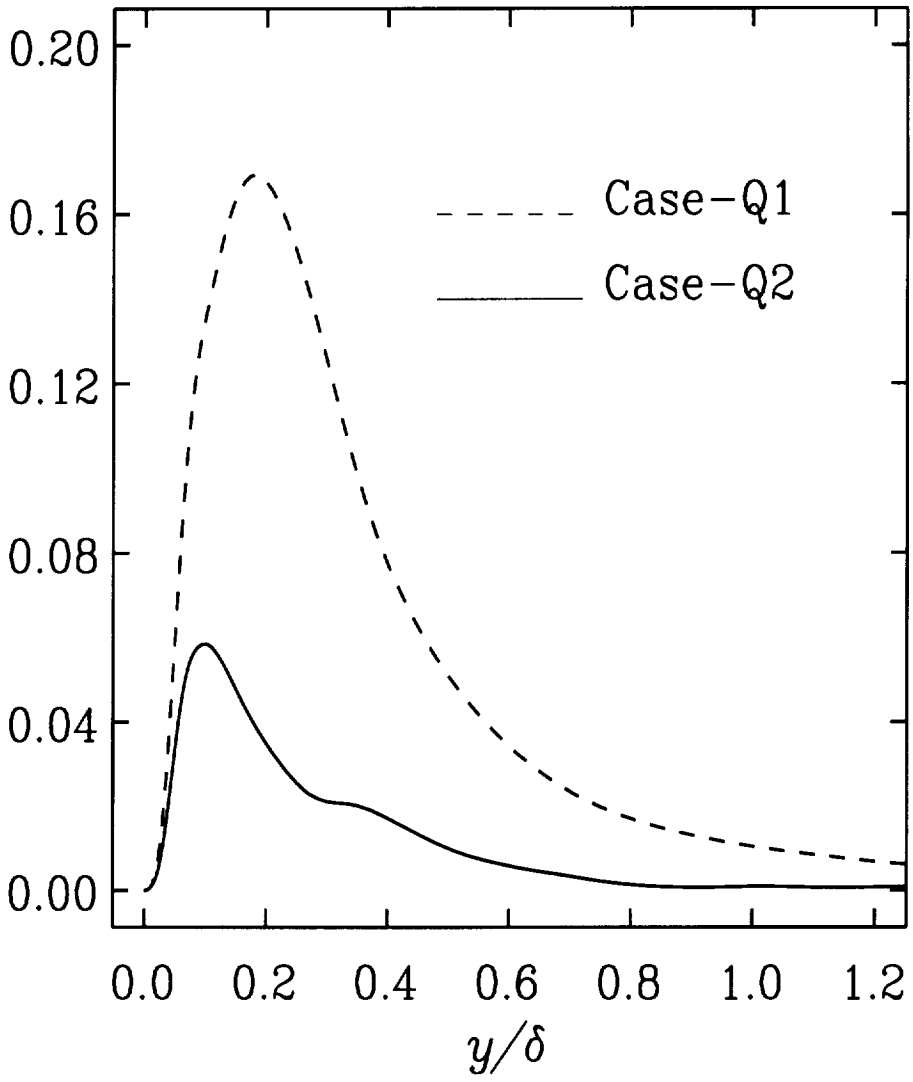

Figure 5: Comparison of $-\overline{u'v'}/u_\tau^2$ distributions with incompressible computations. ····· , $M = 0, Re_{\delta_1} = 500$ (Spalart 1988); — · — , $M = 0, Re_{\delta_1} = 1500$ (Spalart 1988); — ··· —, $M = 0, Re_{\delta_1} = 2000$ (Spalart 1988).

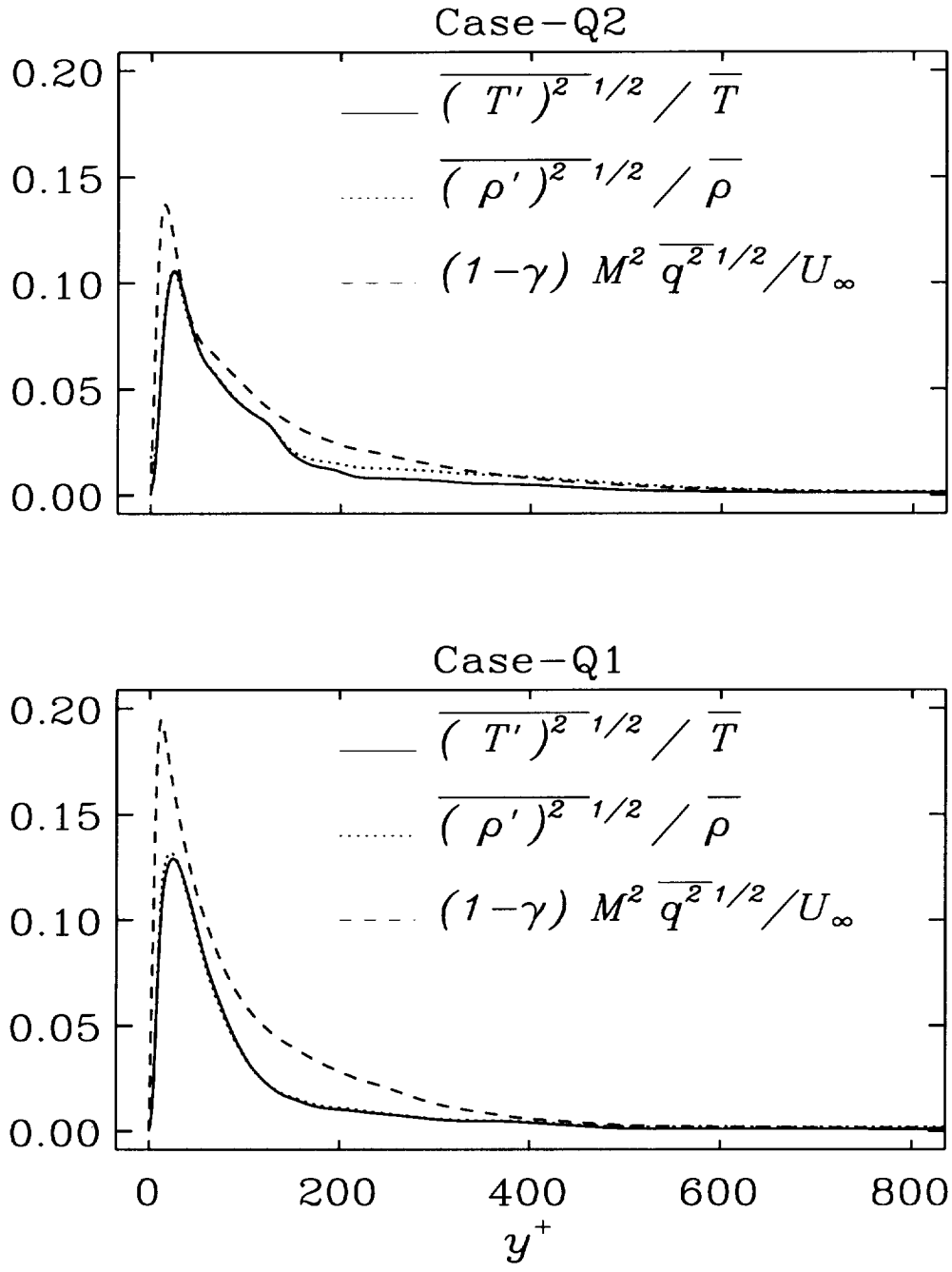

Figure 6: Comparison of density, temperature, and (total) velocity fluctuations.

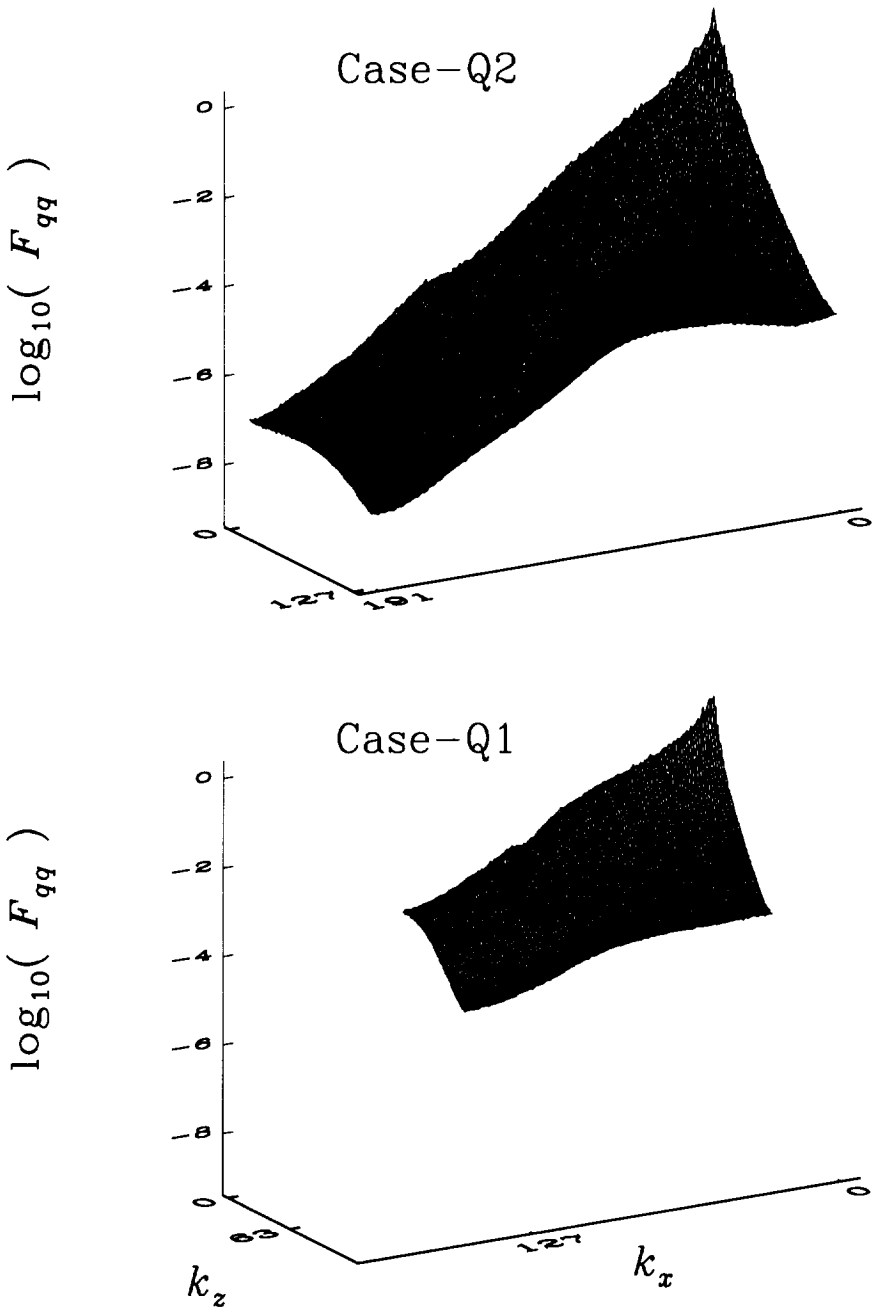

Figure 7: Maximum amplitudes of two-dimensional Fourier spectra of total velocity perturbations.

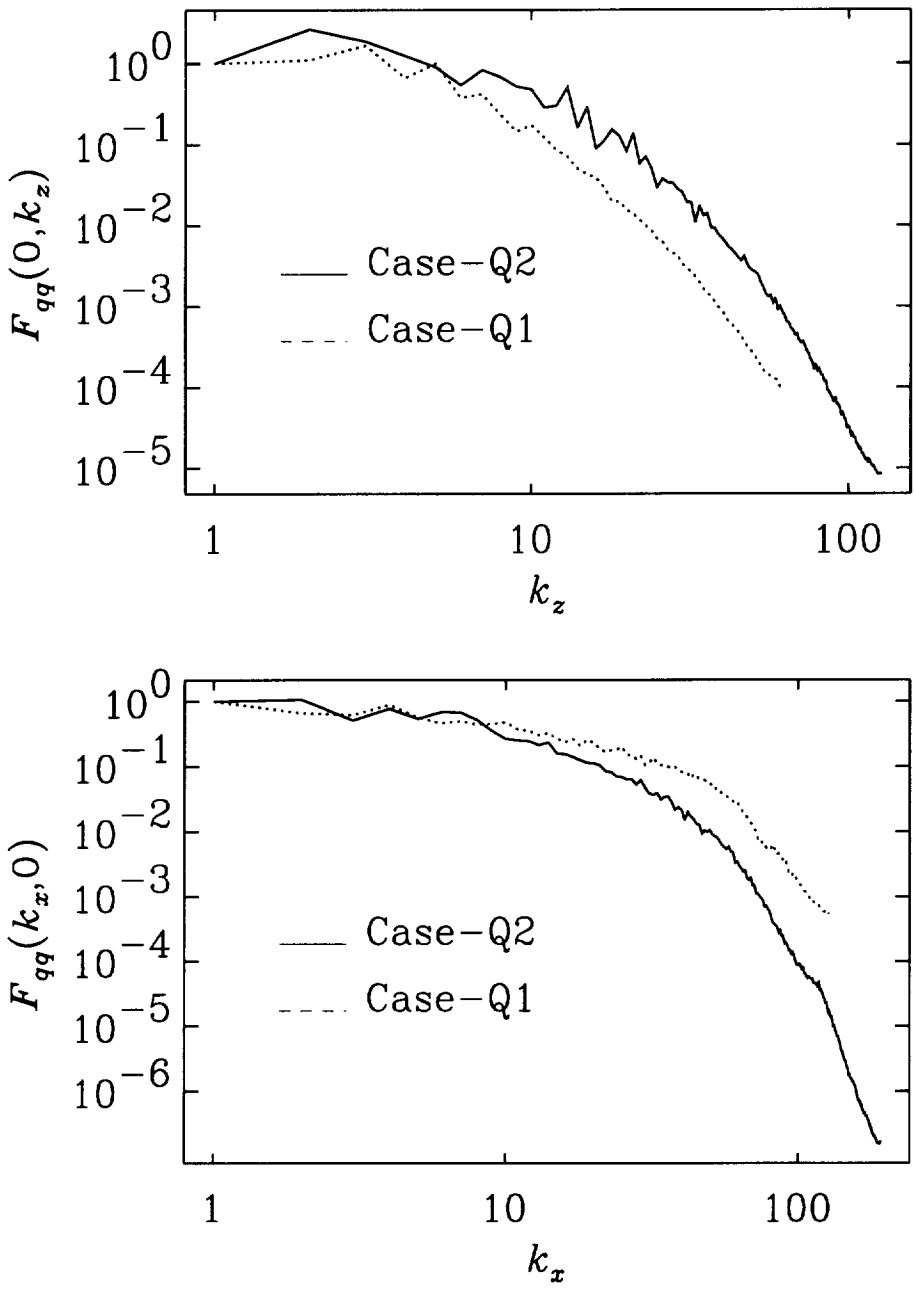

Figure 8: Maximum amplitudes of one-dimensional Fourier spectrum of the total velocity perturbations in the streamwise and spanwise wavenumber space.

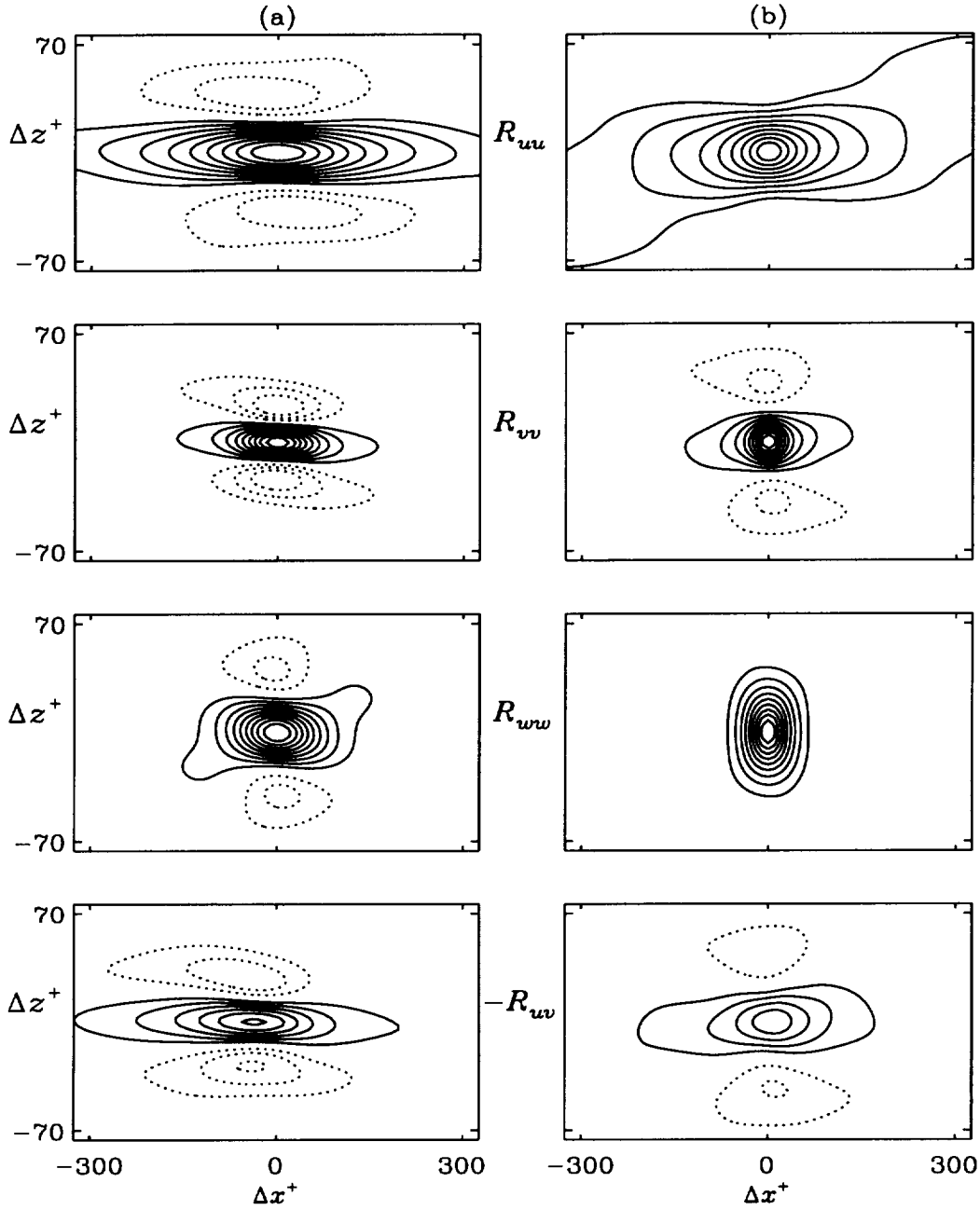

Figure 9: Two-point correlations of the velocity fluctuations with streamwise and spanwise separations, (a) $\boldsymbol{R}(\Delta x^+, \Delta z^+, y_a^+ = 5.98, y_b^+ = 5.98)$, (b) $\boldsymbol{R}(\Delta x^+, \Delta z^+, y_a^+ = 34.60, y_b^+ = 34.60)$. Contour levels with constant increments of 0.1 were shown between -0.5 and 1.0. Zero contour level is suppressed. Solid lines are for the positive contours whilst the dotted lines denote the negative levels.

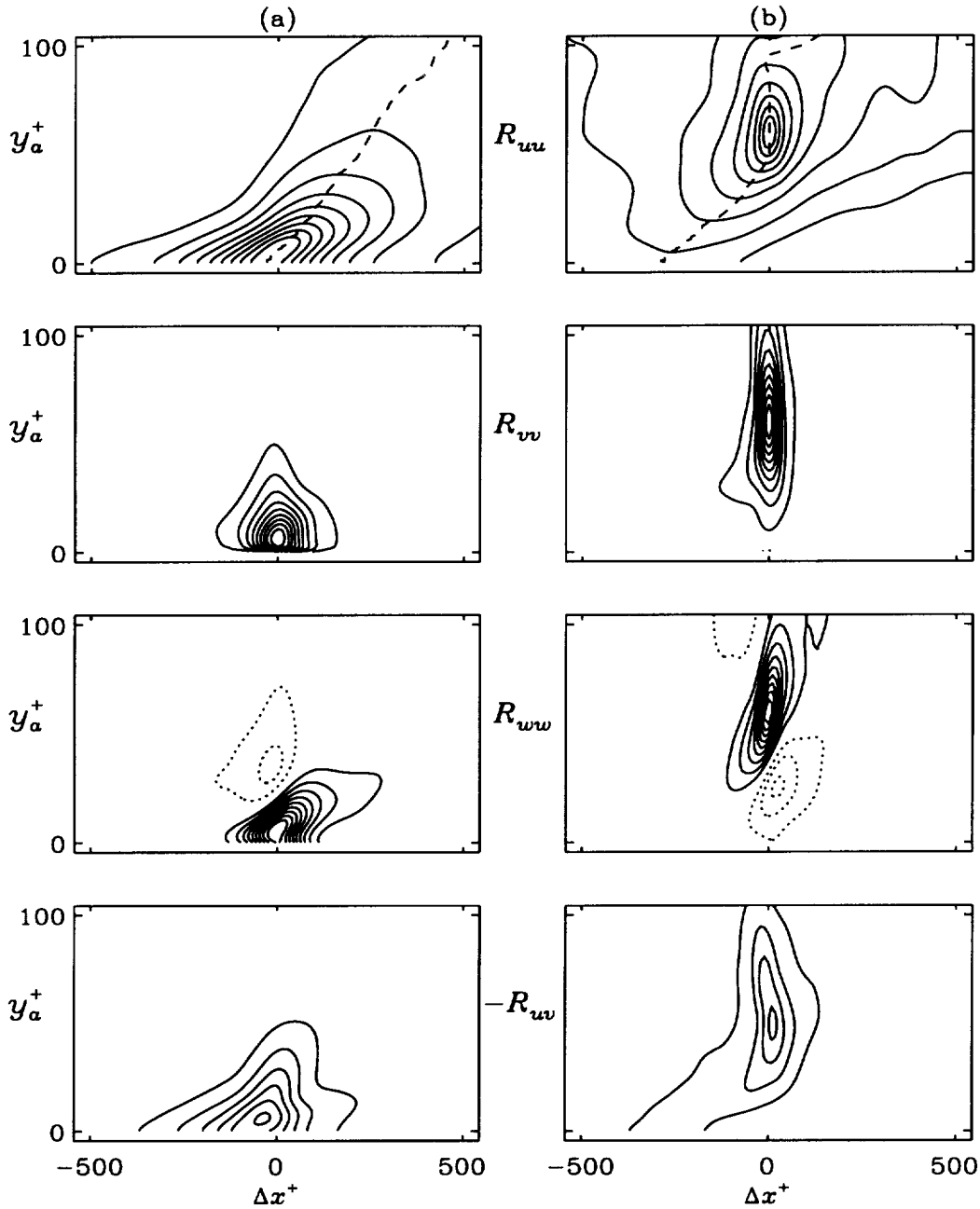

Figure 10: Two-point correlations of the velocity fluctuations with streamwise and wall-normal separations, (a) $\boldsymbol{R}(\Delta x^+, \Delta z^+ = 0, y_a^+, y_b^+ = 5.98)$, (b) $\boldsymbol{R}(\Delta x^+, \Delta z^+ = 0, y_a^+, y_b^+ = 59.75)$. Contour levels with constant increments of 0.1 were shown between -0.5 and 1.0. Zero contour level is suppressed. Solid lines are for the positive contours whilst the dotted lines denote the negative levels.

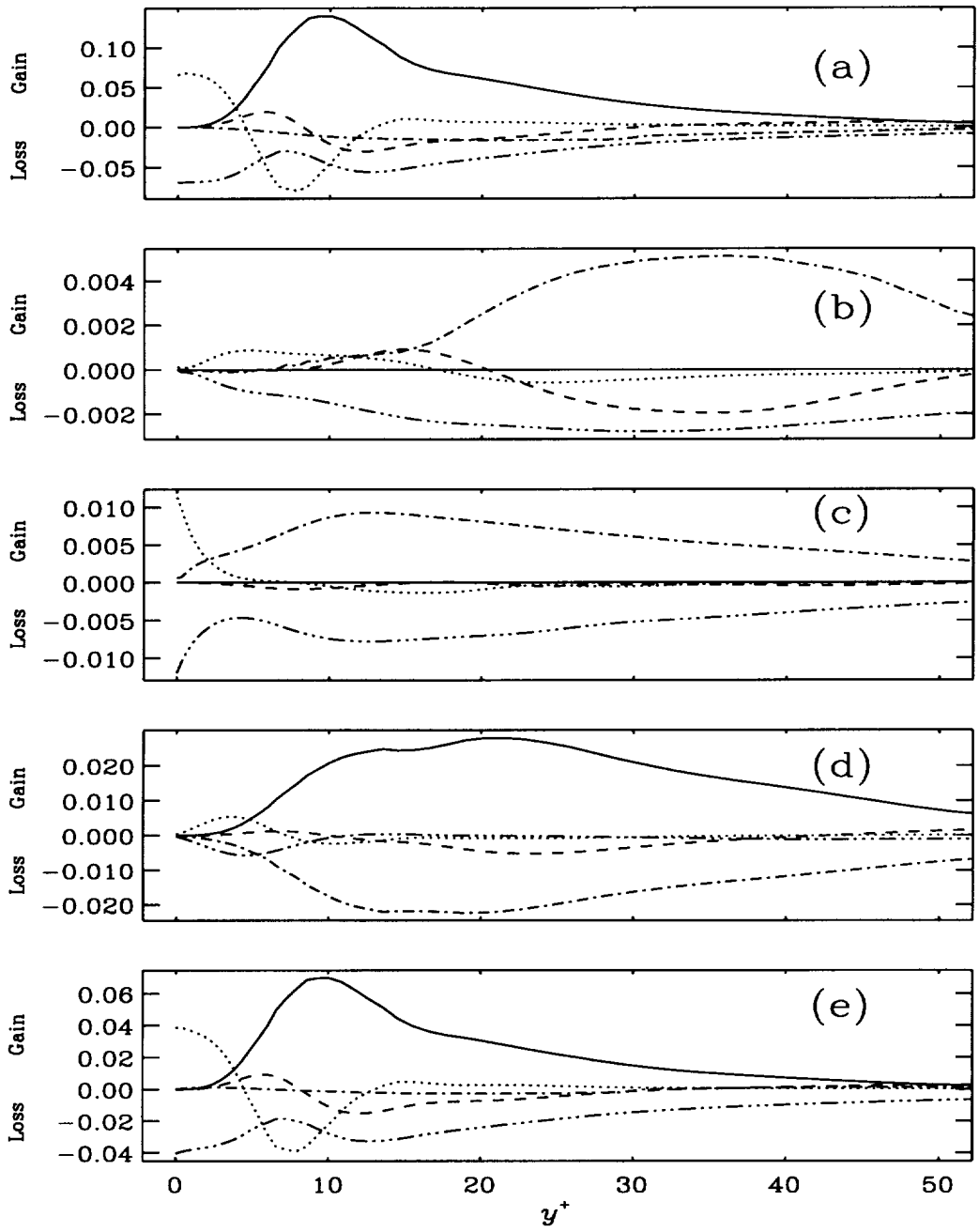

Figure 11: Terms in the near-wall budget in wall coordinates at $M = 2.5$ for (a) $\overline{\rho u''^2}$, (b) $\overline{\rho v''^2}$, (c) $\overline{\rho w''^2}$. (d) $-\overline{\rho u'' v''}$. (e) $\boldsymbol{TKE}$. ——— , production; – – – , turbulent transport; ····· , viscous diffusion; – · – , pressure-gradient/velocity; – ··· –, dissipation.

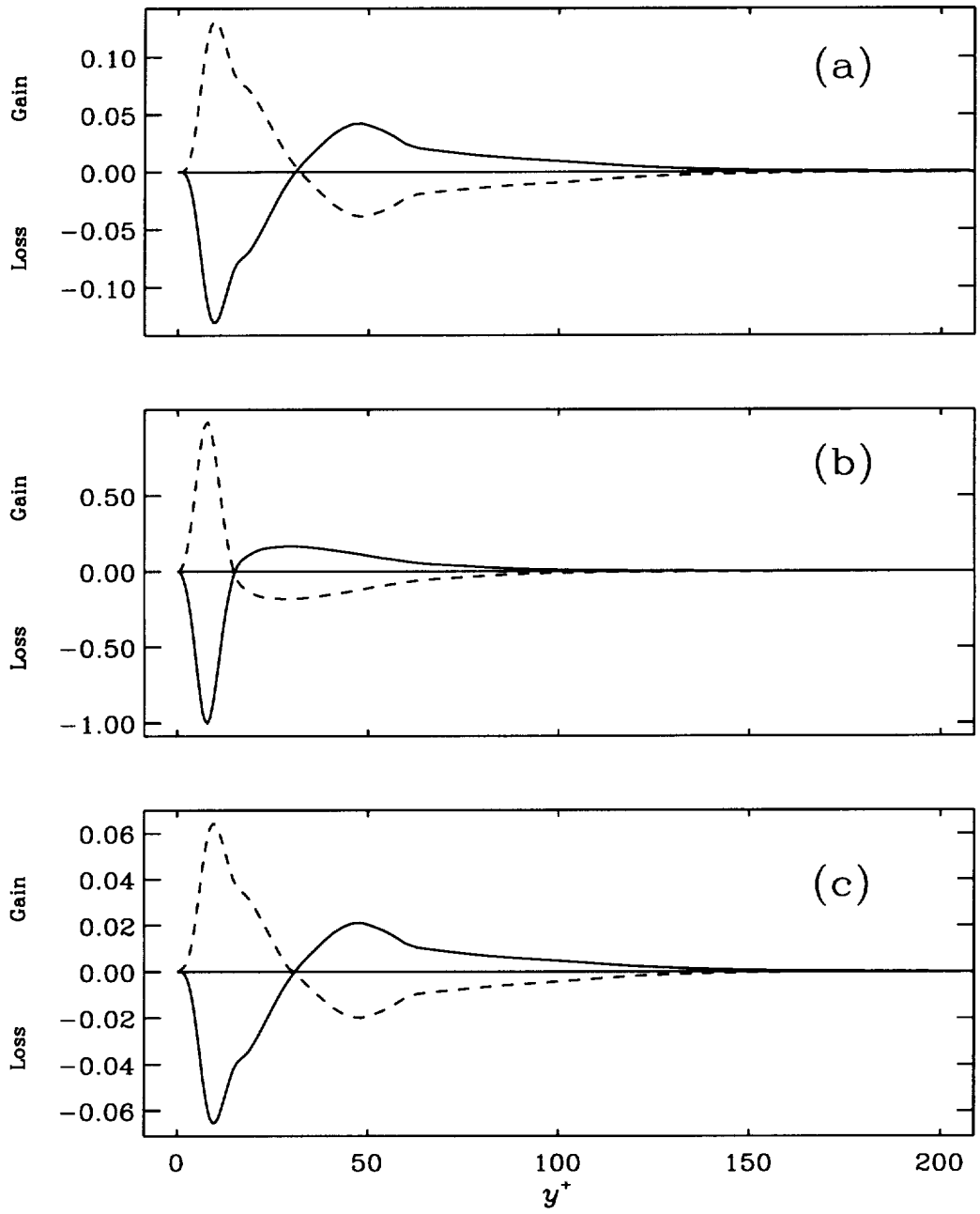

Figure 12: Comparison of the pressure-strain and pressure-diffusion terms in the budget of (a) $\overline{\rho v''^2}$, (b) $-\overline{\rho u'' v''}$, (c) $\boldsymbol{TKE}$. ——, $\boldsymbol{\Theta}$; – – –, $\boldsymbol{\Phi}$.

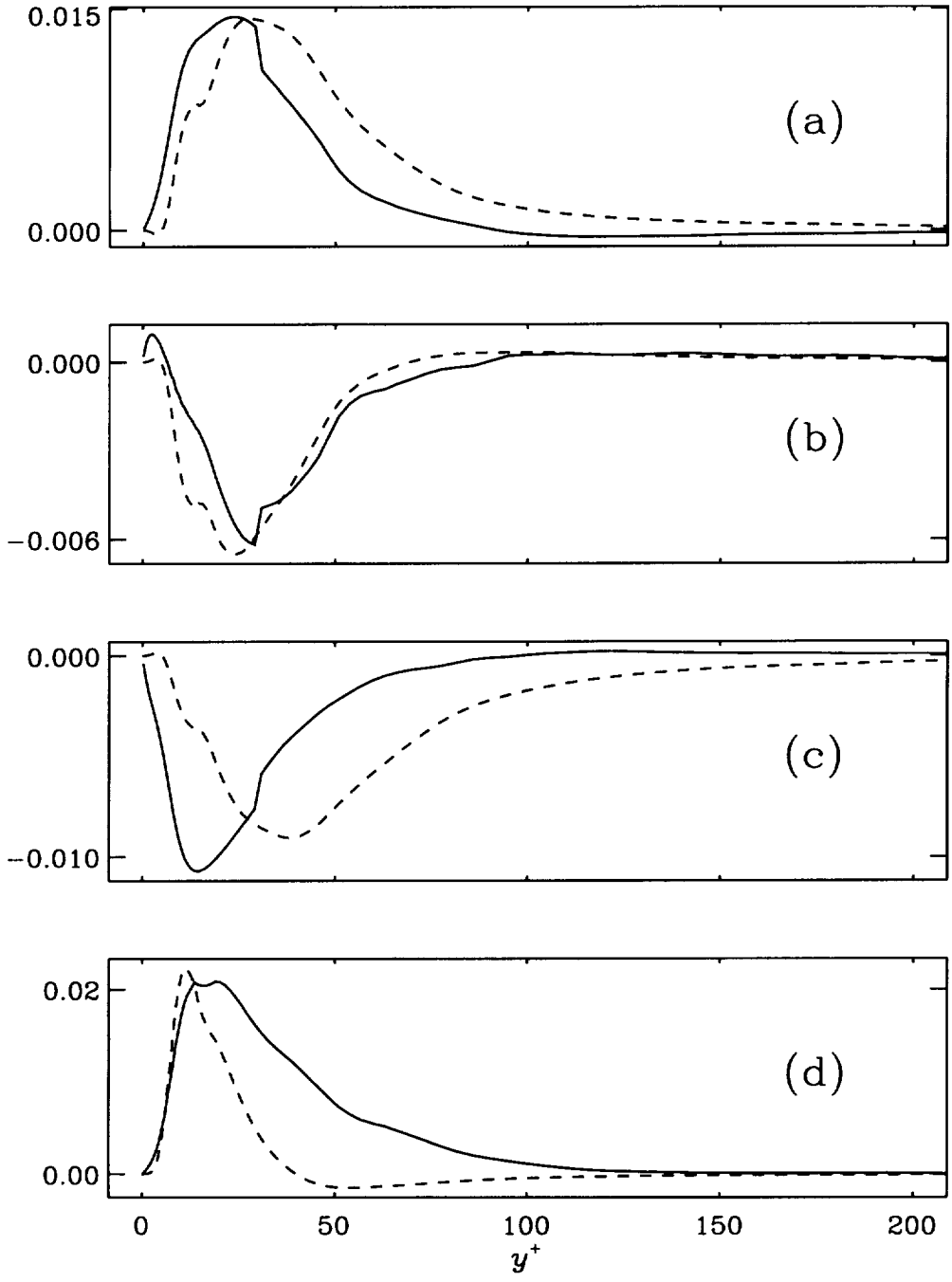

Figure 13: The comparison of the DNS results and SSG model predictions for the deviatoric part of the tensor of pressure-gradient/velocity correlations, (a) Π^d_{11}, (b) Π^d_{22}, (c) Π^d_{33}, (d) Π^d_{12}. ——, DNS; – – –, model.

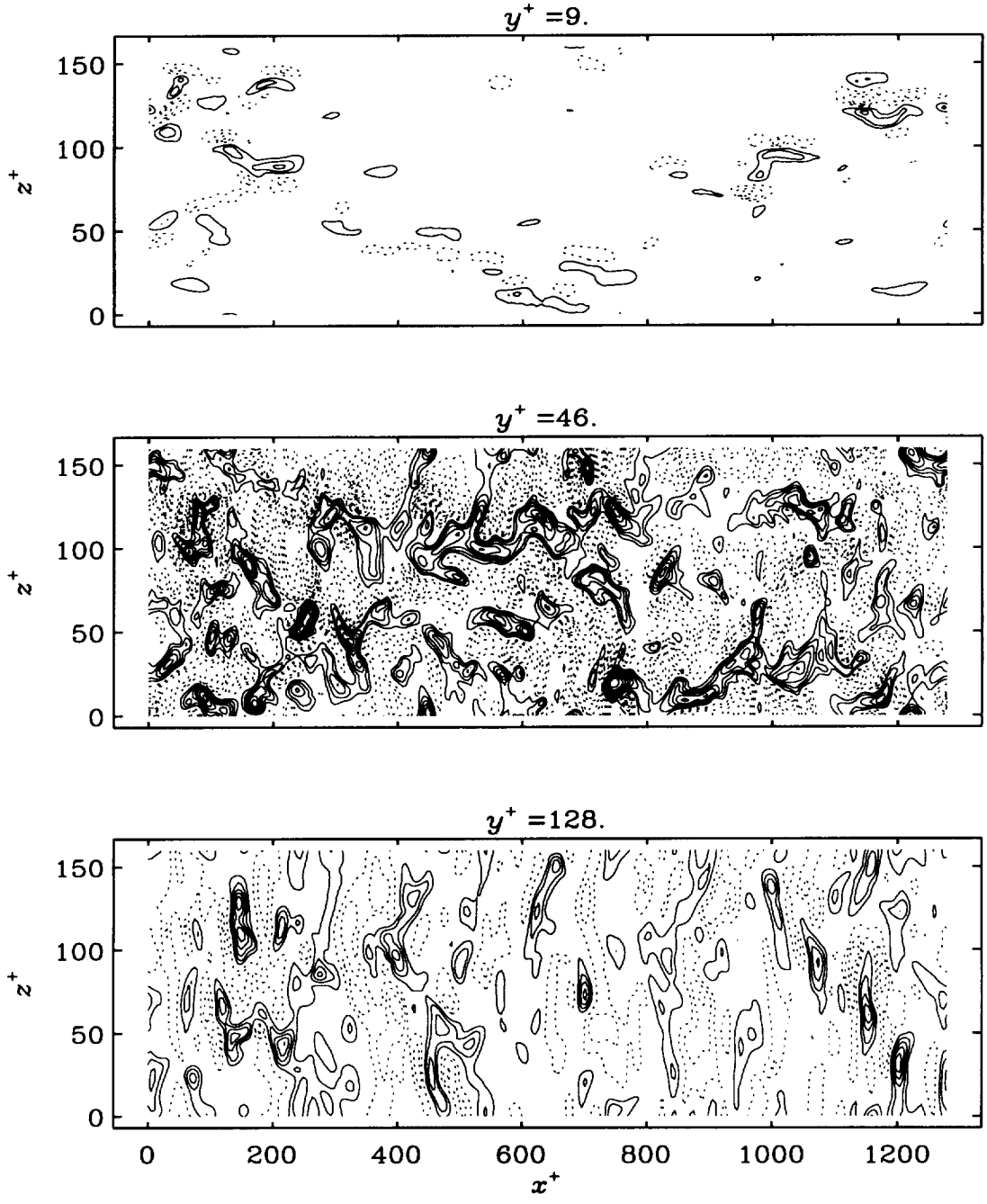

Figure 14: Contours of v^+ in the (x^+, z^+) plane; dotted and solid lines are for negative and positive contours, respectively, and the zero-contour is suppressed. Uniformly spaced 21 contour levels between -2.0 and 2.0 are displayed.

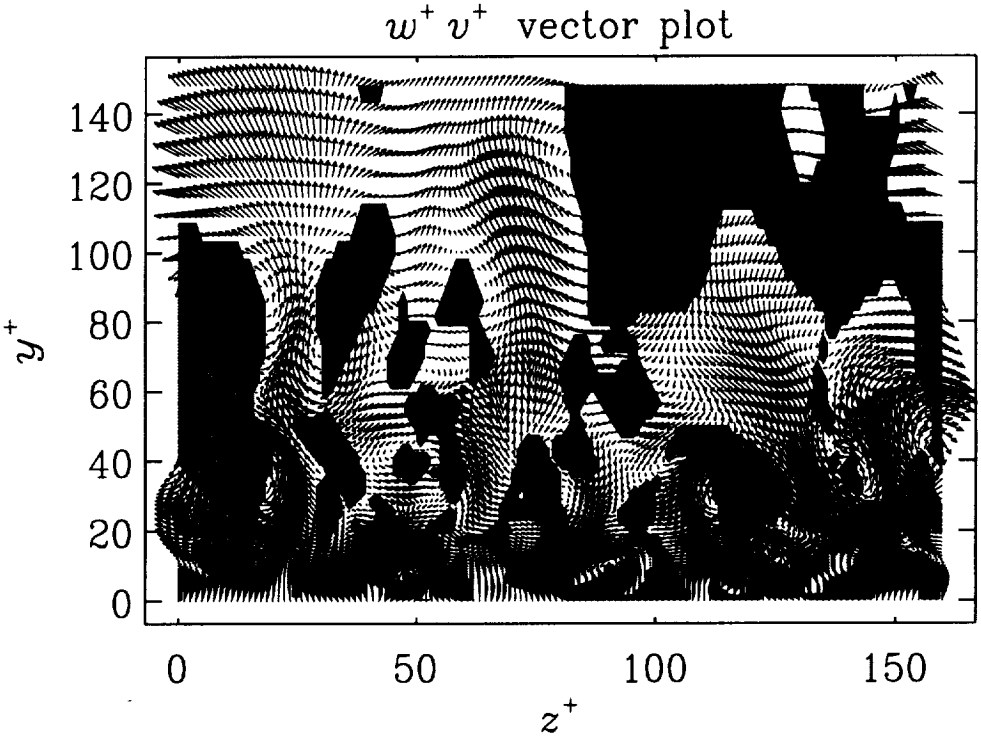

Figure 15: Instantaneous (w^+, v^+) velocity fluctuation vectors in the (z^+, y^+) plane; negative $\boldsymbol{R}_{uv}$ generating motions are colored gray, while negative $\boldsymbol{R}_{uv}$ motions are left white.